PHYSICAL REVIEW D **95,** 095024 (2017)

Dark matter and collider studies in the left-right symmetric model with vectorlike leptons

Sahar Bahrami,[1,*] Mariana Frank,[2,†] Dilip Kumar Ghosh,[3,‡] Nivedita Ghosh,[3,§] and Ipsita Saha[4,‖]

[1]*Department of Physics, McGill University, 3600 Rue University, Montreal, Quebec, Canada H3A 2T8*
[2]*Department of Physics, Concordia University, 7141 Sherbrooke Street West, Montreal, Quebec, Canada H4B 1R6*
[3]*Department of Theoretical Physics, Indian Association for the Cultivation of Science, 2A & 2B, Raja S. C. Mullick Road, Kolkata 700032, India*
[4]*Istituto Nazionale di Fisica Nucleare, Sezione di Roma, Piazzale Aldo Moro 2, I-00185 Roma, Italy*

(Received 10 January 2017; published 30 May 2017)

In the context of a left-right symmetric model, we introduce one full generation of vectorlike lepton doublets (both left- and right-handed) together with their mirror doublets. We show that the lightest vectorlike neutrino in the model is right-handed, and can serve as the dark matter candidate. We find that the relic density as well as the direct and indirect DM detection bounds are satisfied for a large range of the parameter space of the model. In accordance with the parameter space, we then explore the possibility of detecting signals of the model at both the LHC and the ILC, in the pair production of the associated vectorlike charged leptons which decay into final states including dark matter. A comprehensive analysis of signal and backgrounds shows that the signals at the ILC, especially with polarized beams, are likely to be visible for light vectorlike leptons, even with low luminosity, rendering our model highly predictable and experimentally testable.

DOI: 10.1103/PhysRevD.95.095024

I. INTRODUCTION

In left-right symmetric models (LRSMs), left- and right-handed particles are treated on the same footing. This represents an improvement over the Standard Model (SM), where, instead of providing an explanation for its origin, parity violation is incorporated *ad hoc* into the model. Left-right models assume parity is conserved at high energies and broken spontaneously at lower energies, providing an alternative explanation for why nature would prefer any left-right discrimination. In addition, these models have several attractive features, such as providing an explanation for matter-antimatter symmetry, and a natural framework for neutrino masses [1–3]. It is reasonable to ask whether these models can accommodate and explain dark matter (DM), another ingredient missing in the SM.

This topic has been previously explored in the context of LRSMs—for instance, imposing a discrete $Z_2 = (-1)^{3(B-L)}$ symmetry denoted matter parity that survives after the breaking of global $SO(10)$ into $SU(3)_c \otimes SU(2)_L \otimes SU(2)_R \otimes U(1)_{B-L}$. Identifying some representations of $SO(10)$ as Z_2-even, while others are odd, a possible DM candidate can be accommodated where the scalars belonging to the odd representation would represent the DM candidates [4–8]. Alternatively, a Z_2 symmetry can also be imposed such as the triplet scalars (Δ_L and Δ_R) introduced in the model, which will transform under the symmetry as ($\Delta_L \to -\Delta_L$, $\Delta_R \to \Delta_R$). Furthermore, setting the vacuum expectation value (VEV) of the left-handed triplet Δ_L^0 to be zero ($v_L = 0$), the neutral components would become degenerate and stable, and can thus cater possible dark matter candidates. Unfortunately, this Δ_L^0 candidate cannot provide the correct relic density, due to small annihilation cross sections [9]. This problem has been cured by introducing an additional gauge singlet [10]. Leptophilic properties of the decaying left-handed triplet Higgs have been explored to explain enhancements in neutrino-induced muon fluxes [11], and further properties of the gauge singlet have been explored in Ref. [10]. LRSMs with fermionic dark matter have also been explored [12–14].

Here we shall explore an alternative candidate for dark matter—vectorlike neutrinos—by introducing additional vectorlike lepton doublets to LRSMs [15]. Vectorlike fermions appear naturally in composite Higgs models, warped extra dimensions, little Higgs, and extended grand unified theories. In left-right models, where left and right chiral representations are naturally connected, vectorlike fermions are germane, as they are characterized by having left- and right-handed components transforming in the same way under the symmetry group of the theory, and by the fact that the couplings for the right-handed components are the same as for the left-handed ones. Vectorlike fermions have received much attention lately, being put forth as explanations for hints of new physics at the LHC: the ATLAS diboson [16], the CMS $eejj$ excess [17], and the 750 GeV diphoton signal [18,19]. In particular, vectorlike particles in the context of left-right symmetric models

*sahar.bahrami@mail.mcgill.ca
†mariana.frank@concordia.ca
‡tpdkg@iacs.res.in
§tpng@iacs.res.in
‖ipsita.saha@roma1.infn.it

 © 2017 American Physical Society

are inherent in warped space extradimensional models. If the additional dimension, extending between two branes, one at the TeV scale (IR brane) and the other at Planck scale (UV brane), with gravity propagating in the bulk, is warped, the resulting geometry generates naturally the hierarchy between the electroweak scale ($M_{\rm ew} \sim 200\,{\rm GeV}$) and the Planck scale ($M_{\rm Pl} \sim 10^{18}$ GeV) [20,21]. In addition, if one allows the SM fields to propagate in the bulk of the fifth dimension, these models can explain the observed masses of the fermions, with lighter fermions localized near the Planck brane and the heavier ones localized near the TeV brane. Within this new framework, generic models with warped extra dimensions are still very constrained by electroweak and flavor precision tests [22]. To reduce the pressure from electroweak precision tests, a common cure is to enlarge the gauge symmetry of the SM by introducing a custodial $SU(2)_L \times SU(2)_R$ symmetry that limits the corrections to various precision observables [23]. This new symmetry provides a natural framework for vectorlike fermions in LRSMs, which appear as KK excitations of SM chiral fermions.

Vectorlike fermions appear in LRSMs also from gauged flavor symmetries, where they are needed to cancel new gauge anomalies [24]. Additionally, in left-right models, the scale where the parity breaks down, Λ_R, is expected to be high—10^{14} GeV or higher. One could introduce another intermediate mass scale, associated with the $(B-L)$-breaking scale Λ_{B-L} [25], which could emerge as the scale of some new fermions—in our case, the vectorlike leptons—sometimes interpreted as the scale of compositeness [26]. In addition, it is known that in two-Higgs doublet models, vectorlike fermions, in addition to the extra Higgs bosons, alleviate electroweak precision tests [27]. Some collider studies related to such vectorlike leptons augmented in two-Higgs doublets has been explored in Refs. [28–31].

Effects of vectorlike fermions on the couplings of the SM-like 125 GeV Higgs boson, constrained from measurements of the Higgs-production cross sections and branching ratios at the LHC, have been analyzed before [32]. Here, in the context of LRSMs, we seek to examine when they can become dark matter candidates, what is their effect on the parameter space, and how this scenario can be discriminated at the present (LHC) and proposed (ILC) colliders.

Our work is organized as follows: In Sec. II, we describe the LRSM with the addition of vectorlike lepton doublets. For simplicity, we concentrate in particular on scenarios where mixing between ordinary leptons and vectorlike leptons is forbidden by a discrete parity symmetry. The model has one left-handed and one right-handed doublet, and their mirror representations, yielding mixing between same-charge components. We discuss the mass eigenstates, the lightest of which would be the dark matter candidate. In Sec. III, we calculate the relic density, the spin-independent and spin-dependent cross sections, and the annihilation cross section and muon and neutrino fluxes, and we explore the parameter space which is consistent with the experimental results on dark matter detection. In Sec. IV, we explore ways in which this scenario can be tested—in particular, looking for signals of the lightest vectorlike charged lepton pair at the LHC (Sec. IV B) and ILC (Sec. IV C). We summarize our results in Sec. V. In the Appendix, we provide explicit expressions for the vectorlike lepton mass eigenstates.

II. THE LEFT-RIGHT SYMMETRIC MODEL

In the left-right symmetric model [1–3], the Standard Model gauge symmetry is extended to include the gauge group $SU(2)_R$ (with gauge coupling g_R). All right-handed fermions are doublets under this gauge group. Below, we give their quantum numbers under $SU(2)_L \otimes SU(2)_R \otimes U(1)_{B-L}$. The ordinary fermions are the leptons

$$L_{Li} = \begin{pmatrix} \nu_L \\ \ell_L \end{pmatrix}_i \sim (\mathbf{2}, \mathbf{1}, \mathbf{-1}),$$
$$L_{Ri} = \begin{pmatrix} \nu_R \\ \ell_R \end{pmatrix}_i \sim (\mathbf{1}, \mathbf{2}, \mathbf{-1}) \tag{1}$$

and the quarks

$$Q_{Li} = \begin{pmatrix} u_L \\ d_L \end{pmatrix}_i \sim (\mathbf{2}, \mathbf{1}, \mathbf{1/3}),$$
$$Q_{Ri} = \begin{pmatrix} u_R \\ d_R \end{pmatrix}_i \sim (\mathbf{1}, \mathbf{2}, \mathbf{1/3}), \tag{2}$$

where $i = 1, 2, 3$ are generation indices. Note that the right-handed neutrino is automatically included. The electroweak symmetry is broken by the bidoublet Higgs field

$$\Phi \equiv \begin{pmatrix} \phi_1^0 & \phi_2^+ \\ \phi_1^- & \phi_2^0 \end{pmatrix} \sim (\mathbf{2}, \mathbf{2}, \mathbf{0}). \tag{3}$$

In addition, to break the $SU(2)_R \otimes U(1)_{B-L}$ gauge symmetry and to provide Majorana mass terms for neutrinos, we introduce the Higgs triplets

$$\Delta_L \equiv \begin{pmatrix} \delta_L^+/\sqrt{2} & \delta_L^{++} \\ \delta_L^0 & -\delta_L^+/\sqrt{2} \end{pmatrix} \sim (\mathbf{3}, \mathbf{1}, \mathbf{2}),$$
$$\Delta_R \equiv \begin{pmatrix} \delta_R^+/\sqrt{2} & \delta_R^{++} \\ \delta_R^0 & -\delta_R^+/\sqrt{2} \end{pmatrix} \sim (\mathbf{1}, \mathbf{3}, \mathbf{2}). \tag{4}$$

The electric charge is given by $Q = T_L^3 + T_R^3 + \frac{B-L}{2}$. The subscripts L and R are associated with the projection $P_{L,R} = \frac{1}{2}(1 \mp \gamma_5)$. We add one family of vectorlike leptons[1]

[1]Vectorlike quarks can also appear; for the present work, we assume them to be much heavier than the leptons, based on the mass limits [33], and thus they decouple from the low-energy spectrum.

$$L'_L = \begin{pmatrix} \nu'_L \\ \ell'_L \end{pmatrix} \sim (\mathbf{2},\mathbf{1},-\mathbf{1}), \qquad L'_R = \begin{pmatrix} \nu'_R \\ \ell'_R \end{pmatrix} \sim (\mathbf{1},\mathbf{2},-\mathbf{1}),$$
$$L''_R = \begin{pmatrix} \nu''_R \\ \ell''_R \end{pmatrix} \sim (\mathbf{2},\mathbf{1},-\mathbf{1}), \qquad L''_L = \begin{pmatrix} \nu''_L \\ \ell''_L \end{pmatrix} \sim (\mathbf{1},\mathbf{2},-\mathbf{1}), \tag{5}$$

where L'_L and L'_R are new fermion doublets, and L''_R and L''_L are the mirror doublets. Furthermore, using the gauge symmetry to eliminate complex phases, the most general vacuum is

$$\langle \Phi \rangle = \begin{pmatrix} \kappa_1/\sqrt{2} & 0 \\ 0 & \kappa_2 e^{i\alpha}/\sqrt{2} \end{pmatrix},$$
$$\langle \Delta_L \rangle = \begin{pmatrix} 0 & 0 \\ v_L e^{i\theta_L}/\sqrt{2} & 0 \end{pmatrix},$$
$$\langle \Delta_R \rangle = \begin{pmatrix} 0 & 0 \\ v_R/\sqrt{2} & 0 \end{pmatrix}. \tag{6}$$

Note that only Δ_R is needed for symmetry breaking, and Δ_L is included to preserve left-right symmetry. We assume, as is usual for LRMs, $v_L \ll v_R$ to obtain light left-handed neutrino masses, and $\kappa_2 < \kappa_1$ to avoid potentially large flavor violation coming from the Higgs sector. The Lagrangian density for this model contains—in addition to the SM terms—kinetic and Yukawa terms for ordinary leptons, explicit terms for the vectorlike leptons, and potential terms:

$$\mathcal{L}_{\rm LRM} = \mathcal{L}_{\rm kin} + \mathcal{L}_Y + \mathcal{L}_{\rm VL} - V(\Phi, \Delta_L, \Delta_R), \tag{7}$$

where

$$\begin{aligned} L_{\rm kin} = i\sum \bar{\psi}\gamma^\mu D_\mu \psi = {} & \bar{L}'_L \gamma^\mu \left(i\partial_\mu + g_L \frac{\vec{\tau}}{2}\cdot \vec{W_{L\mu}} - \frac{g'}{2} B_\mu \right) L'_L \\ & + \bar{L}'_R \gamma^\mu \left(i\partial_\mu + g_R \frac{\vec{\tau}}{2}\cdot \vec{W_{R\mu}} - \frac{g'}{2} B_\mu \right) L'_R \\ & + \bar{L}''_L \gamma^\mu \left(i\partial_\mu + g_R \frac{\vec{\tau}}{2}\cdot \vec{W_{R\mu}} - \frac{g'}{2} B_\mu \right) L''_L \\ & + \bar{L}''_R \gamma^\mu \left(i\partial_\mu + g_L \frac{\vec{\tau}}{2}\cdot \vec{W_{L\mu}} - \frac{g'}{2} B_\mu \right) L''_R, \end{aligned} \tag{8}$$

where we introduce the gauge fields $\vec{W}_{L,R}$ and B corresponding to $SU(2)_{L,R}$ and $U(1)_{B-L}$. They mix with the following matrices [34]:

$$\begin{pmatrix} W_L^\pm \\ W_R^\pm \end{pmatrix} = \begin{pmatrix} \cos\xi & \sin\xi e^{i\alpha} \\ -\sin\xi e^{-i\alpha} & \cos\xi \end{pmatrix} \begin{pmatrix} W_1^\pm \\ W_2^\pm \end{pmatrix}. \tag{9}$$

The angle ξ characterizes the mixing between left- and right-handed gauge bosons, with $\tan 2\xi = -\frac{2\kappa_1\kappa_2}{v_R^2 - v_L^2}$. It follows that

$$\xi \simeq -\kappa_1\kappa_2/v_R^2 \simeq -2\frac{\kappa_2}{\kappa_1}\left(\frac{m_{W_L}}{m_{W_R}}\right)^2, \tag{10}$$

so that the mixing angle ξ is at most[2] the square of the ratio of the left and right scales $(\Lambda_L/\Lambda_R)^2$. Here $\Lambda_L \simeq 10^2$ GeV corresponds to the electroweak scale, and $\Lambda_R \simeq$ TeV is the scale of parity breaking, v_R.

With negligible mixing, the gauge boson masses become, for $g_L = g_R$,

$$m_{W_L} \simeq m_{W_1} \simeq \frac{g}{2}\kappa_+ \quad \text{and} \quad m_{W_R} \simeq m_{W_2} \simeq \frac{g}{\sqrt{2}} v_R, \tag{11}$$

with $\kappa_+^2 = \kappa_1^2 + \kappa_2^2$. The model also has an additional neutral gauge boson, Z_R, which mixes with the Standard Model Z boson. The mass eigenstates $Z_{1,2}$ acquire masses

$$m_{Z_1} \simeq \frac{g}{2\cos\theta_W}\kappa_+ \simeq \frac{m_{W_1}}{\cos\theta_W} \quad \text{and}$$
$$m_{Z_2} \simeq \frac{g\cos\theta_W}{\sqrt{\cos 2\theta_W}} v_R \simeq \sqrt{\frac{2\cos^2\theta_W}{\cos 2\theta_W}} m_{W_2}, \tag{12}$$

where $g = e/\sin\theta_W$ and with the $U(1)_{B-L}$ coupling constant $g_{B-L} \equiv e/\sqrt{\cos 2\theta_W}$. Again, one expects the mixing between the neutral gauge bosons to be of order $(\Lambda_L/\Lambda_R)^2$—i.e.,

$$\begin{aligned} \sin 2\phi &= -\frac{g^2\kappa_+^2\sqrt{\cos 2\theta_W}}{2c_W^2(m_{Z_2}^2 - m_{Z_1}^2)} \simeq -\frac{2m_{Z_1}^2\sqrt{\cos 2\theta_W}}{m_{Z_2}^2 - m_{Z_1}^2} \\ &\simeq -2\sqrt{\cos 2\theta_W}\left(\frac{m_{Z_1}}{m_{Z_2}}\right)^2. \end{aligned} \tag{13}$$

Equations (11) and (12) imply that $m_{Z_2} \simeq 1.7 m_{W_2}$ [37,38]. The appropriate gauge coupling constants are g_s, $g_L = g_R$ and $g' = g_{B-L}$, respectively. The right-handed $SU(2)_R$-breaking scale is restricted from low-energy observables, such as $K_L - K_S$, ϵ_K, $B^0 - \bar{B}^0$ mixings, and $b \to s\gamma$ processes where the right-handed charged current contributes significantly [34,39–48]. Thus, these processes provide a bound to the scale v_R by means of the charged right-handed W_R boson mass as well as the LR Higgs masses. In particular, the right-handed W_R mass is restricted to be greater than 3 TeV, while the heavy bidoublet Higgs mass should at least be 10 TeV [34]. In our study, we thus fix the scale v_R at 10 TeV.

[2]Although the experimental limit is $\xi < 10^{-2}$ [33], for $m_{W_R} = \mathcal{O}(\text{TeV})$, one has $\xi \leq 10^{-3}$ [35]; supernova bounds for right-handed neutrinos lighter than 1 MeV are even more stringent ($\xi < 3 \times 10^{-5}$) [35,36].

The rest of the Lagrangian terms,

$$\mathcal{L}_Y = -[Y_L \bar{L}_L \Phi L_R + Y_R \bar{L}_R \Phi L_L + \tilde{Y}_L \bar{L}_L \tilde{\Phi} L_R + \tilde{Y}_R \bar{L}_R \tilde{\Phi} L_L + h_{L_{ij}} \overline{L_L^{ic}} i\tau_2 \Delta_L L_L^j + h_{R_{ij}} \overline{L_R^{ic}} i\tau_2 \Delta_R L_R^j + \text{H.c.}], \quad (14)$$

are the Yukawa interaction terms for the ordinary leptons, where $Y_{L,R}$, $\tilde{Y}_{L,R}$ are 3×3 complex matrices; $h_{L_{ij}}$, $h_{R_{ij}}$ are 3×3 complex symmetric Yukawa matrices; and $\tilde{\Phi} = \tau_2 \Phi^\star \tau_2$. Additionally, with the vectorlike family of leptons as defined above, the Lagrangian describing Yukawa interaction terms for vectorlike fermions and their interactions with ordinary fermions, and allowing for both Dirac and Majorana mass terms, is

$$\begin{aligned}\mathcal{L}_{\text{VL}} = -[&M_L \bar{L}'_L L''_R + M_R \bar{L}'_R L''_L + Y'_L \bar{L}'_L \Phi L'_R + Y'_R \bar{L}''_R \Phi L''_L + \tilde{Y}'_L \bar{L}'_L \tilde{\Phi} L'_R + \tilde{Y}'_R \bar{L}''_R \tilde{\Phi} L''_L \\ &+ h'_L \overline{L'^c_L} i\tau_2 \Delta_L L'_L + h''_R \overline{L''^c_L} i\tau_2 \Delta_R L''_L + h'_R \overline{L'^c_R} i\tau_2 \Delta_R L'_R + h''_L \overline{L''^c_R} i\tau_2 \Delta_L L''_R + \lambda'^i_L \bar{L}'_L \Phi L^i_R \\ &+ \lambda'^i_R \bar{L}^i_L \tilde{\Phi} L'_R + \lambda''^i_L \overline{L^{ic}_L} i\tau_2 \Delta_L L'_L + \lambda''^i_R \overline{L^{ic}_R} i\tau_2 \Delta_R L'_R + \lambda'''^i_L \overline{L^{ic}_L} i\tau_2 \Delta_L L''_R + \lambda'''^i_R \overline{L^{ic}_R} i\tau_2 \Delta_R L''_L + \text{H.c.}]. \end{aligned} \quad (15)$$

Here, in addition to the new Yukawa couplings $Y'_{L,R}$, $Y''_{L,R}$ of the vectorlike leptons with the bidoublet; and $h'_{L,R}$, $h''_{L,R}$, the Yukawa couplings of the vectorlike leptons with triplet $\Delta_{L,R}$; we also introduce explicit mass terms for the vectorlike leptons M_L and M_R. The scalar potential for the bidoublet Φ and triplet $\Delta_{L,R}$ Higgs fields is

$$\begin{aligned} V(\phi, \Delta_L, \Delta_R) = &-\mu_1^2(\text{Tr}[\Phi^\dagger \Phi]) - \mu_2^2(\text{Tr}[\tilde{\Phi}\Phi^\dagger] + (\text{Tr}[\tilde{\Phi}^\dagger \Phi])) - \mu_3^2(\text{Tr}[\Delta_L \Delta_L^\dagger] + \text{Tr}[\Delta_R \Delta_R^\dagger]) + \lambda_1((\text{Tr}[\Phi\Phi^\dagger])^2) \\ &+ \lambda_2((\text{Tr}[\tilde{\Phi}\Phi^\dagger]) + (\text{Tr}[\tilde{\Phi}^\dagger \Phi])^2) + \lambda_3(\text{Tr}[\tilde{\Phi}\Phi^\dagger]\text{Tr}[\tilde{\Phi}^\dagger \Phi]) + \lambda_4(\text{Tr}[\Phi\Phi^\dagger](\text{Tr}[\tilde{\Phi}\Phi^\dagger] + \text{Tr}[\tilde{\Phi}^\dagger \Phi])) \\ &+ \rho_1((\text{Tr}[\Delta_L \Delta_L^\dagger])^2 + (\text{Tr}[\Delta_R \Delta_R^\dagger])^2) + \rho_2(\text{Tr}[\Delta_L \Delta_L]\text{Tr}[\Delta_L^\dagger \Delta_L^\dagger] + \text{Tr}[\Delta_R \Delta_R]\text{Tr}[\Delta_R^\dagger \Delta_R^\dagger]) \\ &+ \rho_3(\text{Tr}[\Delta_L \Delta_L^\dagger]\text{Tr}[\Delta_R \Delta_R^\dagger]) + \rho_4(\text{Tr}[\Delta_L \Delta_L]\text{Tr}[\Delta_R^\dagger \Delta_R^\dagger] + \text{Tr}[\Delta_L^\dagger \Delta_L^\dagger]\text{Tr}[\Delta_R \Delta_R]) \\ &+ \alpha_1(\text{Tr}[\Phi\Phi^\dagger](\text{Tr}[\Delta_L \Delta_L^\dagger] + \text{Tr}[\Delta_R \Delta_R^\dagger])) + \alpha_2(\text{Tr}[\Phi\tilde{\Phi}^\dagger]\text{Tr}[\Delta_R \Delta_R^\dagger] + \text{Tr}[\Phi^\dagger \tilde{\Phi}]\text{Tr}[\Delta_L \Delta_L^\dagger]) \\ &+ \alpha_2^*(\text{Tr}[\Phi^\dagger \tilde{\Phi}]\text{Tr}[\Delta_R \Delta_R^\dagger] + \text{Tr}[\tilde{\Phi}^\dagger \Phi]\text{Tr}[\Delta_L \Delta_L^\dagger]) + \alpha_3(\text{Tr}[\Phi\Phi^\dagger \Delta_L \Delta_L^\dagger] + \text{Tr}[\Phi^\dagger \Phi \Delta_R \Delta_R^\dagger]) \\ &+ \beta_1(\text{Tr}[\Phi \Delta_R \Phi^\dagger \Delta_L^\dagger] + \text{Tr}[\Phi^\dagger \Delta_L \Phi \Delta_R^\dagger]) + \beta_2(\text{Tr}[\tilde{\Phi} \Delta_R \Phi^\dagger \Delta_L^\dagger] + \text{Tr}[\tilde{\Phi}^\dagger \Delta_L \Phi \Delta_R^\dagger]) \\ &+ \beta_3(\text{Tr}[\Phi \Delta_R \tilde{\Phi}^\dagger \Delta_L^\dagger] + \text{Tr}[\Phi^\dagger \Delta_L \tilde{\Phi} \Delta_R^\dagger]), \end{aligned} \quad (16)$$

where we follow Ref. [49] and explicitly indicate the complex parameters. The parameters can be further reduced and simplified by making use of the symmetries of the model. Assuming a discrete left-right symmetry in addition to the left-right gauge symmetry, the $SU(2)$ gauge couplings become equal ($g_L = g_R = g$), and the Yukawa coupling matrices for the left- and right-handed sectors in the model are related. With a discrete parity symmetry ($L'_L \leftrightarrow L'_R$, $L''_L \leftrightarrow L''_R$, $\Phi \leftrightarrow \Phi^\dagger$, $\Delta_L \leftrightarrow \Delta_R^*$), it follows that $h'_{L,R} = h''^\star_{L,R}$, $Y'_L = Y_L{}'^\star$, $\tilde{Y}_L = \tilde{Y}'^\dagger_L$, $Y'_R = Y_R{}'^\star$, $\tilde{Y}_R = \tilde{Y}'^\dagger_R$. In addition, using the charge conjugation symmetry we obtain $h'_{L,R} = h''_{L,R} \equiv h$. New symmetries can be introduced to restrict the interactions of the vector leptons. For instance, we can impose *(i)* a symmetry under which all the new $SU(2)_R$ doublet fields are odd, while the new $SU(2)_L$ doublets are even, which forces all Yukawa couplings involving new fermions to vanish, $Y'_L = \tilde{Y}'_L = Y'_R = \tilde{Y}'_R = 0$, and the vector fermion masses arise only from explicit terms in the Lagrangian [50]; and/or *(ii)* a new parity symmetry which disallows mixing between the ordinary fermions and the new fermion fields, under which all the new vectorlike fields are odd, while the others are even [51], such that $\lambda'^i_L = \lambda'^i_R = \lambda'''^i_L = \lambda'''^i_R = 0$. The latter symmetry is important for light vectorlike leptons, as this scenario would satisfy restrictions from lepton-flavor-violating decays, which otherwise would either force the new leptons to be very heavy, ~10–100 TeV, or else reduce the branching ratio for the Higgs into dileptons to 30%–40% of the SM prediction [51,52]. In addition, if all vectorlike fermions are odd under the new parity symmetry, the lightest particle can become stable and act as all, or part of, the dark matter in the Universe. Thus, in what follows, we will perform the analysis under the simplifying assumption *(ii)*.

A. Constraints on model parameters

Current bounds on additional gauge bosons are derived from their hadronic and leptonic decay channels, and constraints are obtained from both ATLAS and CMS searches [53,54]. These are quite restrictive, with the W_R and Z_R masses being constrained to lie above, or about, 2.7 TeV. In our numerical investigations we choose

$v_R = 10$ TeV, and thus the W_R and Z_R masses remain high, with $M_{W_R} = 4.2$ TeV. Furthermore, we assume $v_L < 5$ GeV, which agrees with the limits from the electroweak precision constraints; see Refs. [55,56] for the Higgs triplet model, and Ref. [57] for the LRSM.

The left-handed doubly charged Higgs bosons $H_L^{\pm\pm}$ can be light in general LRSM scenarios. The masses of these doubly charged scalars are strongly restricted by the LHC searches for same-sign dilepton (electron or muon) signatures, while the bound is less stringent for ditau final states [58–60]. However, the experiments tend to assume 100% branching ratios for each of the leptonic final states. Thus, the constraints can be softened by assuming small couplings to leptons. In addition, allowing them to decay into vectorlike leptons would also modify the mass limits. In our case, $H_L^{\pm\pm}$ decay mostly into $W_L^{\pm}W_L^{\pm}$ pairs, with a branching ratio of 85%. We take $M_{H_L^{\pm\pm}} = 300$ GeV, which obeys all the experimental bounds. Our analysis does not particularly focus on the scalar sector of the model, and the masses can be independently taken at high value without affecting our searches for the vectorlike leptons, as is also explained in the following sections.

B. Vectorlike leptons

The spectrum from Eq. (5) now consists of, in the charged sector, a (2×2)-dimensional mass matrix $\mathcal{M}_c$. Note that here, as in the case of the neutral vectorlike leptons studied below, the matter parity symmetry introduced in this section forbids mixing with the ordinary fermions, and thus the mass matrix in the charged sector is just 2×2, while in the neutral sector it is 4×4.

$$(\bar{e}'_L \bar{e}''_L)(\mathcal{M}_c)\begin{pmatrix} e'_R \\ e''_R \end{pmatrix}, \text{ with } \mathcal{M}_c = \begin{pmatrix} m'_E & M_L \\ M_R & m''_E \end{pmatrix}, \tag{17}$$

with $m'_E = \frac{Y'^e_L \kappa_2 e^{i\alpha} + \tilde{Y}'^e_L \kappa_1}{\sqrt{2}}$ and $m''_E = \frac{Y'^e_R \kappa_2 e^{i\alpha} + \tilde{Y}'^e_R \kappa_1}{\sqrt{2}}$, from the Lagrangian Eq. (16). The mass matrix can be diagonalized by two unitary matrices U^L and U^R as follows:

$$U^{L\dagger}\mathcal{M}_c U^R = \begin{pmatrix} M_{E_1} & 0 \\ 0 & M_{E_2} \end{pmatrix}. \tag{18}$$

The mass eigenvalues are (by convention, the order is $M_{E_1} > M_{E_2}$ [50,61])

$$M^2_{E_1,E_2} = \frac{1}{2}\left[(M_L^2 + m'^2_E + M_R^2 + m''^2_E) \pm \sqrt{(M_L^2 + m'^2_E - M_R^2 - m''^2_E)^2 + 4(m''_E M_L + m'_E M_R)^2}\right]. \tag{19}$$

In the neutral sector, the mass matrix is

$$\frac{1}{2}(\bar{\nu'_L}\, \bar{\nu'^c_R}\, \bar{\nu''^c_R}\, \bar{\nu''_L})(\mathcal{M}_\nu)\begin{pmatrix} \nu'^c_L \\ \nu'_R \\ \nu''_R \\ \nu''^c_L \end{pmatrix}, \quad \text{with}$$

$$\mathcal{M}_\nu = \begin{pmatrix} \sqrt{2}h'_L v_L e^{i\theta} & m'_\nu & M_L & 0 \\ m'_\nu & M'_\nu & 0 & M_R \\ M_L & 0 & \sqrt{2}h''_L v_L e^{i\theta} & m''_\nu \\ 0 & M_R & m''_\nu & M''_\nu \end{pmatrix}, \tag{20}$$

with Dirac masses $m'_\nu = \frac{Y'^\nu_L \kappa_1 + \tilde{Y}'^\nu_L \kappa_2 e^{-i\alpha}}{\sqrt{2}}$, $m''_\nu = \frac{Y'^\nu_R \kappa_1 + \tilde{Y}'^\nu_R \kappa_2 e^{-i\alpha}}{\sqrt{2}}$, and with Majorana masses $M'_\nu = h'_R v_R/\sqrt{2}$ and $M''_\nu = h''_R v_R/\sqrt{2}$. This mass matrix can be diagonalized by a unitary matrix V:

$$V^\dagger \mathcal{M}_\nu V = \begin{pmatrix} M_{\nu_1} & 0 & 0 & 0 \\ 0 & M_{\nu_2} & 0 & 0 \\ 0 & 0 & M_{\nu_3} & 0 \\ 0 & 0 & 0 & M_{\nu_4} \end{pmatrix}. \tag{21}$$

Exact analytic expressions are difficult to find.[3] To simplify, we work in the limit where $h''_R = Y'^\nu_R = \tilde{Y}'^\nu_R = 0$ (meaning $M''_\nu = m''_\nu = 0$). In the limit where $m'_\nu \ll M_L, M_R$, the neutrino mass matrix can be diagonalized, yielding four neutrino masses:

$$M_{\nu_{1,2}} = \frac{M'_\nu}{2} \mp \sqrt{\frac{M'^2_\nu}{4} + M_R^2 + m'^2_\nu}, \tag{22}$$

$$M_{\nu_{3,4}} = \pm M_L, \tag{23}$$

valid to $\mathcal{O}(m'^2_\nu/M_L)$. The lightest of these states will be the dark matter candidate, which, as it is odd under the additional parity symmetry *(ii)*, is stable. The lightest state will depend on assumptions made on the masses M_L, M_R and triplet Yukawa couplings h'_R and Y'_L. We also must choose the parameters carefully in the charged sector, to insure that the charged vectorlike leptons are heavier than the neutral ones. Taking into account the constraints $M_{E_2} \geq 101.9$ GeV [33] by LEP, this requirement is not difficult to satisfy. Moreover, we analyzed the constraints on the parameter space and found that for a fixed $Y'^\nu_L (= 1.5)$ (our benchmark BP1 value from Sec. IV IV A), there is a narrow region of very small

[3] In our analyses, we use exact numerical expressions, and we show here approximate analytical expressions for clarity.

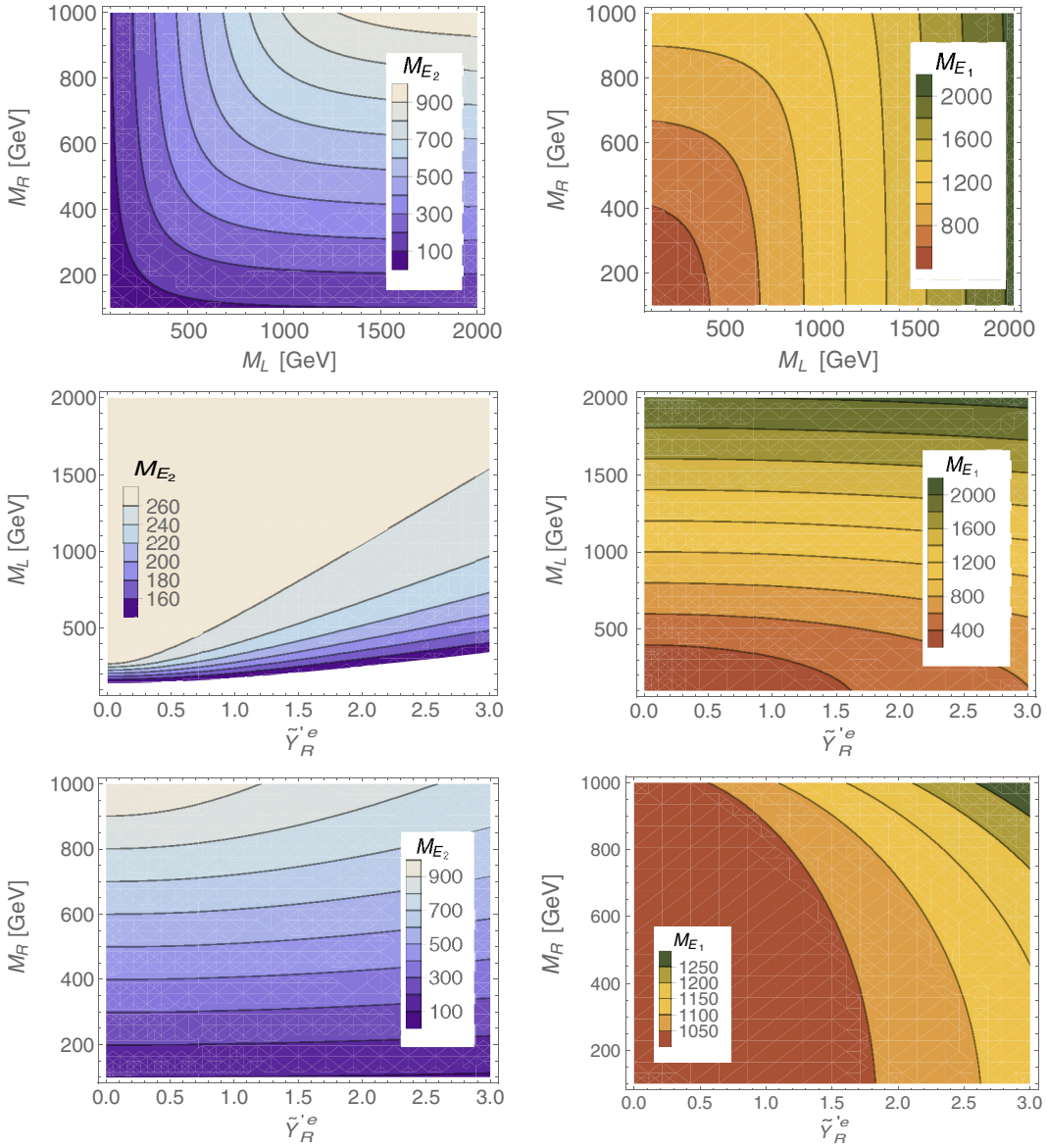

FIG. 1. *Left panel:* Contour plots showing the dependence of the lightest vectorlike charged lepton masses (M_{E_2}) on M_L, M_R for $\tilde{Y}'^e_R = 2.5$ (top); on $M_L, \tilde{Y}'^e_R$ for $M_R = 275$ GeV (middle); and on $M_R, \tilde{Y}'^e_R$ for $M_L = 1000$ GeV (bottom). *Right panel:* Same contour graphs showing the dependence of the heavier vectorlike charged lepton mass (M_{E_1}). We take the Yukawa couplings $Y'^e_L = 0.1$, $Y'^e_R = 2.5$. The panels on the right indicate the color-coded mass values for the contours.

$h'_R (0 < h'_R < 0.04)$ for the range of $M_R \in (150\ \text{GeV}–1\ \text{TeV})$, for which the charged VL lepton is lighter than the neutral one. We exclude these points.[4] In the limit in which $M_L \gg M_R$, there are two heavy (approximately) degenerate eigenvalues of mass M_L, which do not mix with the lighter states ν_1 and ν_2. In this limit, the lightest state is ν_1, and it is mostly the ν''_L state, with some admixture of ν'^c_R, and is right-handed.

Some comments about this analysis:

(1) If we require $M'_\nu = m'_\nu = 0$ instead of $M''_\nu = m''_\nu = 0$, there is no difference in the final result, but we have m''_ν in the mass expressions replacing m'_ν.

(2) If we set $M'_\nu = m'_\nu = 0$, we flip between the $'$ and the $''$ states, and the lightest vectorlike neutrino will be ν'_L.

(3) In our scenario, the states with mass M_L are heavier and decay into lighter vectorlike leptons, making them unsuitable to be DM candidates.

(4) It is advantageous that we get a right-handed neutrino to be the DM candidate, as it is more likely to produce a relic density in the desired range. The left-handed vectorlike neutrino, much like the ordinary one, annihilates too fast through the s channel mediated by the Z_L boson, resulting in a large

[4]In practice, the software we use gives a warning at points where the DM candidate is charged.

annihilation cross section. On the contrary, the right-handed candidate can annihilate through Z_R, which is quite heavy (TeV), and through the Higgs scalars (doublet and triplet). In our case, the DM neutrino candidate is mostly right-handed, but it contains a small mixture of left-handed components, and thus it has a small (but nonzero) coupling to the Z_L boson. Because this mixing is small, the Higgs Yukawa coupling controls the relic density as well as the direct-detection cross section for light right-handed vectorlike neutrinos. Thus, the relic density for such right-handed neutrinos can easily be tuned to within the right ballpark. In addition, the direct-detection cross section will stay in the experimentally allowed region, which is otherwise violated by the left-handed neutrinos due to their large coupling with Z_L. In our scenario, the dominant annihilation processes for right-handed vectorlike neutrinos through the Higgs mediation yield the correct relic density (within the 2σ limit of Planck results) and do not violate the experimental bounds on the direct-detection cross section in the specified regions of the parameter space, making this neutrino a good DM candidate. We return to this in more detail in Secs. III A and III C.

We now explore the parametric dependence of heavy vectorlike leptons in this model. While varying some of the parameters, we fix other parameters, mostly to values that we choose as benchmark points in our following studies. We shall discuss the benchmark points and corresponding parameters in a later section.

In Figs. 1 and 2, we show the mass dependence of the charged vectorlike leptons (both E_2 and E_1) on the various parameters of the model. Specifically, we show the contour plots of M_{E_2} and M_{E_1} in the (M_L, M_R) plane and in the planes correlating M_L and M_R individually to the Yukawa couplings $\tilde{Y}'^{e}_{L}$ and $\tilde{Y}'^{e}_{R}$. We observe that for the same set of parameter ranges, the lighter charged VL lepton mass (M_{E_2}) can at most reach 1 TeV, while the mass of the heavier state (M_{E_1}) cannot be lower than 1 TeV. In this regard, we should mention that while scanning over the mass ranges, we impose the direct search limit on $M_{E_2} > 101.9$ GeV given by LEP [33]. We also note that, as the plots indicate, the lightest vectorlike lepton E_2 is mostly right-handed, while the heavier one E_1 is mostly left-handed. We note that M_{E_2} is the most sensitive to the parameters $\tilde{Y}'^{e}_{R}$ and M_R, while M_{E_1} is the most sensitive to the parameters $\tilde{Y}'^{e}_{L}$ and M_L.

In Fig. 3, we plot the dependences on the parameter space for the vectorlike neutrino masses (M_{ν_1} and M_{ν_2}). Here ν_1 is

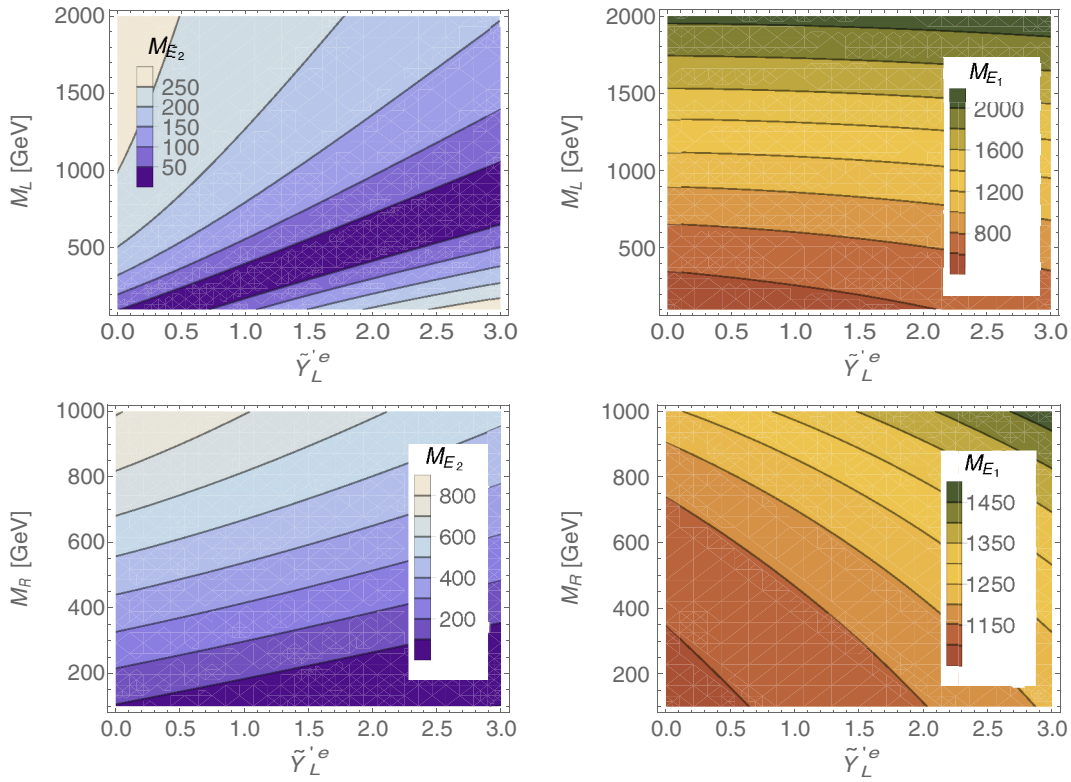

FIG. 2. *Left panel:* Contour plots showing the dependence of the lightest vectorlike charged lepton masses (M_{E_2}) on $M_L, \tilde{Y}'^{e}_{L}$ for $M_R = 275$ GeV (top) and on $M_R, \tilde{Y}'^{e}_{L}$ for $M_L = 1$ TeV (bottom). *Right panel:* Same contour graphs, but for the heavier vectorlike charged lepton mass (M_{E_1}). As before, $Y'^{e}_{L} = 0.1$, $Y'^{e}_{R} = 2.5$, and the panels on the right indicate the color-coded mass values for the contours.

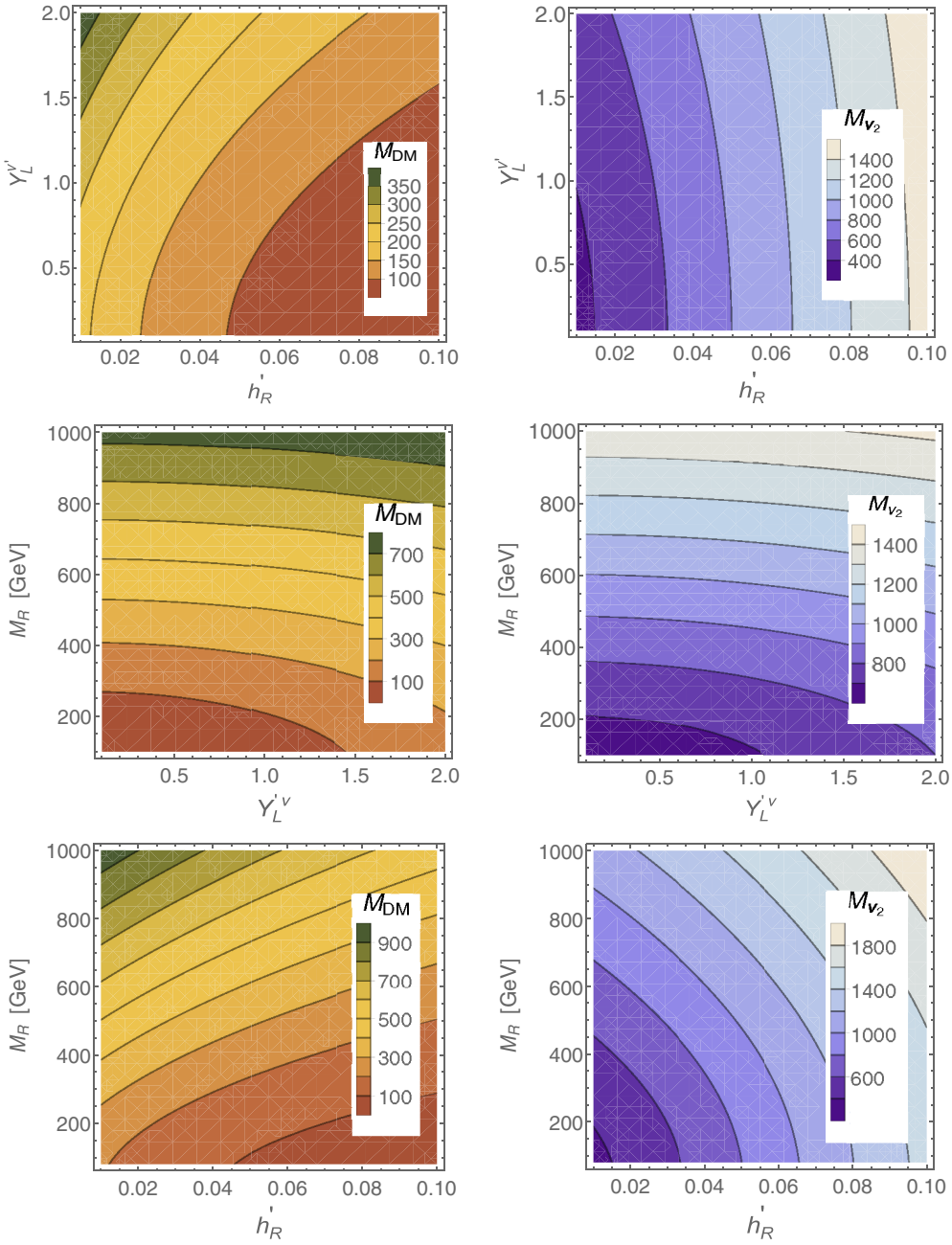

FIG. 3. Contour graphs showing the dependence of the vectorlike neutrino mass, for the lightest state ν_1 (left panel) and for the heavier state ν_2 (right panel) as a function of $Y_L'^{\nu}$ and h_R', with $M_R = 275$ GeV (top), as a function of M_R and $Y_L'^{\nu}$ for $h_R' = 0.045$ (middle), and as a function of M_R and h_R' for $Y_L'^{\nu} = 1.5$ (bottom). The panels on the right indicate the color-coded mass values for the contours.

the lightest neutrino state and the DM candidate (the brown-colored graphs on the left), and the second vectorlike lightest neutrino is ν_2 (the blue-colored contours on the right). The variation is shown only with the relevant parameters—namely, the bare mass terms M_L and M_R, which tune the masses of these neutral VL lepton candidates—and with the Yukawa couplings $Y_L'^{\nu}$ and h_R', which control the DM annihilation cross section and set its relic density. In consequence to the parameter scanning, we now proceed to our analysis on DM sector and collider signatures.

III. DARK MATTER

For the vectorlike neutrino to be a viable candidate for dark matter, it must satisfy conditions of providing the right level of relic abundance from thermal dark matter production in the early Universe. In addition, as the lack of any dark matter signals in either direct or indirect dark matter detection experiments confront our theoretical expectations, these must satisfy increasingly severe constraints from experiments. For the dark matter analysis, we extend

the left-right model in Ref. [62] to include vectorlike leptons using FeynRules [63] and extract the resulting file in CalcHEP [64] to implement the model into micrOMEGAs [65]. We use micrOMEGAs to calculate the relic density ($\Omega_{\rm DM}h^2$), the spin-independent cross section (σ^{SI}), the annihilation cross section ($\langle\sigma v\rangle$), and the neutrino and muon fluxes, which are the most constrained observables for our model. We analyze these in turn below.

A. Relic density

First, we analyze the consequences of having the lightest vectorlike neutrino as our dark matter candidate. Using the results in the previous sections, we explore the parameter space of the model which yields the correct relic density of dark matter, determined very precisely as the amount of nonbaryonic dark matter in the energy-matter of the Universe to be $\Omega_{\rm DM}h^2 = 0.1199 \pm 0.0027$ [66], with $\Omega_{\rm DM}$ being the energy density of the dark matter with respect to the critical energy density of the Universe, and h being the reduced Hubble parameter.

In Fig. 4, we show the 2σ allowed range of relic density: $0.1144 \leq \Omega_{\rm DM}h^2 \leq 0.1252$, as constrained by WMAP [67] and Planck [66], in the $(M_{\rm DM}, M_{E_2^\pm})$ plane by varying $Y_L^{\nu\prime}$ and fixing $h_R' = 0.045$. It should be mentioned here that $M_{E_2^\pm}$ is directly related to M_R, while $M_{\rm DM}$ depends on M_R, h_R', and $Y_L^{\nu\prime}$. Consequently, the DM relic density depends mainly upon model parameters M_R, h_R', and $Y_L^{\nu\prime}$, while the annihilation cross section is most sensitive to $Y_L^{\prime\nu}$, the DM coupling to the SM Higgs doublet. For low $M_{\rm DM}$, the dominant contribution to the DM annihilation cross section comes from the s-channel diagram where the DM pair self-annihilate through the neutral SM Higgs mediation. As

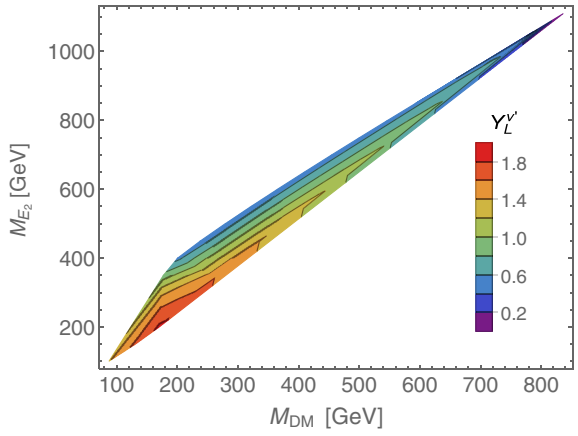

FIG. 4. Contour plots for the allowed relic density as a function of the vectorlike lepton mass M_{E_2} and the vectorlike neutrino (the dark matter candidate) mass (in GeV) for $M_L = 1$ TeV. We impose the restriction $0.1144 \leq \Omega_{\rm DM}h^2 \leq 0.1252$. The color code for the Yukawa coupling $Y_L^{\nu\prime}$ is indicated on the right. All the other parameters are fixed at our BP1 values in Table II.

$M_{\rm DM}$ increases, t-channel contributions (via the DM itself) to $Z_L h$ annihilation modes become dominant.

In Fig. 4, the contours indicate the parameter region that respects the relic constraints for the range of $Y_L^{\prime\nu}$, shown in the color-coded column on the right. It is to be noted here that the mass splittings $(M_{E_2^\pm} - M_{\rm DM})$ can be small only for a small range of allowed parameter space near $Y_L^{\nu\prime} \gtrsim 1.7$. For the rest of the parameter space, the allowed mass splitting is quite large. Coannihilation of the DM candidate with other states does not occur in this scenario, since the other heavy states (ν_2, ν_3, ν_4) are much heavier than the DM candidate. On the other hand, coannihilation with the vectorlike charged leptons $E_2^\pm$ would happen only if the mass splitting can be as low as 3–4 GeV. However, the inclusion of both the 2σ upper and lower bounds on relic density constraints evades the possibility of having a small mass difference between $E_2^\pm$ and DM (3–4 GeV), as this can only yield an under-abundant DM relic.

B. Direct detection

Direct-detection experiments look for signals emerging from dark matter scattering off normal matter (neutrons or protons). As the dark matter only interacts weakly, such events are very rare, and direct-detection experiments require very accurate background rejection. However, these are important, as the expected signals test the nature of the dark matter.

The interaction of dark matter with detector nuclear matter can be spin dependent or spin independent. The spin-dependent scattering can only happen with odd-numbered nucleons in the nucleus of the detector material, while in spin-independent (scalar) scattering, the coherent scattering of all the nucleons in the nucleus with the DM are added in phase. Consequently, in direct-detection experiments, the experimental sensitivity to spin-independent (SI) scattering is much larger than the sensitivity to spin-dependent scattering, which experiences an enhancement in scattering from large target nuclei. In our case, the Z, Z_R boson mediators influence the former, while Higgs boson exchanges usually dominate the latter. The most stringent bounds on the spin-independent σ_{SI} cross section in terms of the dark matter mass come from the XENON100 [68] and LUX [69] experiments, which have seen no dark matter interaction events yet. We explore the spin-independent cross section and compare this against the constraints from XENON100 (dashed blue curve), the LUX experiment (dashed pink curve) and the projected XENON1T (dashed yellow curve) in Fig. 5, where, on the left, we plot the spin-independent dark matter cross section from direct searches as a function of the dark matter mass. As seen in the figure, the cross section predicted by our model (continuous red curve) mostly lies below the experimental bounds for $M_{\rm DM}$ values between 87.4 GeV and 836.5 GeV (the exact region where we get the correct relic density), except in the region 70–150 GeV, where our theoretical expectations lie within

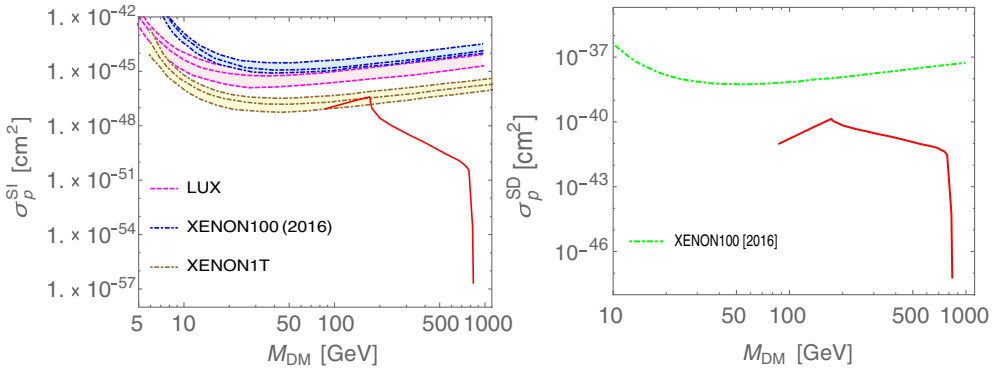

FIG. 5. *Left:* Spin-independent cross section of the proton as a function of the dark matter mass in the left-right symmetric model with vectorlike leptons (red curve), and the experimental upper limits from XENON100 [68] (dashed blue curve), from LUX [69] (dashed pink curve), and from XENON1T [70], all with 2σ expected sensitivity (dashed yellow curve). *Right:* Spin-dependent cross section as a function of the dark matter mass (red curve) and the experimental limit from XENON100 [68]. We include only points in the parameter space where relic density constraints are satisfied. All the other parameters are fixed at our BP1 values in Table II.

the 2σ expected sensitivity from XENON1T [70]. Note that in Fig. 5, the scattering cross section drops suddenly for masses around $M_{\rm DM} \simeq 600$ GeV. The reason lies in the fact that we have plotted *only* those points that satisfy the relic constraints. Scanning over the parameters, we found that it was difficult to satisfy relic constraints for a variety of Yukawa couplings, and whenever possible, we looked for the largest scattering cross section. Increased precision may rule out lower-dark-matter regions of the parameter space. On the right, we plot the spin-dependent cross section, and the recent experimental limit from XENON100 [68]: the constraints imposed are much milder, and our cross section is smaller than the bound imposed by the data by 1–2 orders of magnitude.

C. Indirect detection

Indirect-detection experiments look for signals arising from pair annihilation of dark matter particles into SM particles. There are large number of final states that can be looked at, including $\mu^+, \bar{d}, \bar{p}, \gamma$-line, and γ-continuum spectra. Since our dark matter candidate is primarily right-handed, the Higgs bosons (especially Δ_R^0), the Z, and the Z_R can all act as mediators and enhance the dark matter pair annihilation cross section into fermion pairs. The coupling between the dark matter particle and SM mediators must produce an acceptable annihilation rate and, besides satisfying direct-detection constraints, must be sufficient to produce the correct relic density.

The most stringent constraints on dark matter annihilation cross sections have been derived from the Fermi gamma-ray space telescope (Fermi-LAT) [71], used to search for dark matter annihilation products from dwarf spheroidal galaxies and the Galactic Center, which probe annihilation cross sections into photons. To obtain the correct value for the dark matter density, the annihilation cross section should be $\langle \sigma v \rangle \sim 3 \times 10^{-26}$ cm^3/s. In Fig. 6, we show the annihilation cross section of dark matter as a function of the dark matter mass $M_{\rm DM}$ and compare it with the constraints on the dark matter annihilation cross section for the most restrictive channels, $\mu^+\mu^-$, $b\bar{b}$, and especially the W^+W^- channels, at 95% C.L., found from examining continuum gamma-ray spectra from the dwarf spheroidal galaxy Segue I [71,72]. The red line shows a sudden drop at high mass values, which is due to our choice of discrete points that satisfy the relic density constraints, similar to our previous case for the direct-detection cross section. For light $M_{\rm DM}$ ($\lesssim$100–115 GeV), the dominant annihilation mode is into $b\bar{b}$ (90%) (through the SM-like Higgs), while for larger $M_{\rm DM}$ (from 120 GeV up to 800 GeV), $Z_L h$

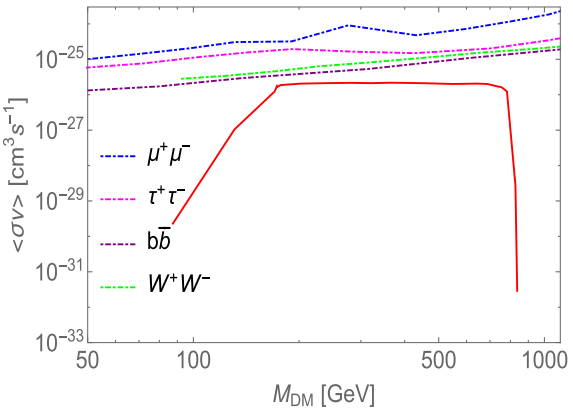

FIG. 6. Annihilation cross section of dark matter into SM particles as a function of the dark matter mass (red curve). We compare this with the combined indirect-detection limits from Fermi-LAT and the MAGIC Collaboration on gamma rays arising from annihilations in dwarf spheroidal galaxies [72]. The dashed curves represent annihilation into $\mu^+\mu^-$ (blue), $\tau^+\tau^-$ (pink), $b\bar{b}$ (purple), and W^+W^- (green). We include only points in the parameter space where relic density constraints are satisfied. All the other parameters are fixed at our BP1 values in Table II.

becomes the dominant annihilation mode (again, about 90%) because of DM annihilation through the t channel. We note that a substantial region of the parameter space survives the limits from indirect detection, although in the region $M_{\rm DM} \in (175\text{–}300)$ GeV, our theoretical prediction is close to the experimental limits.

The dark matter can annihilate into cosmic rays, over much different annihilation channels, for processes which are model dependent. The emission of most particles can be modeled by using leptonic scenarios equally as well as hadronic scenarios. This ambiguity does not exist for high-energy neutrinos, as they can be created efficiently only in hadronic interactions via the decay of charged pions. The detection of a high-energy astrophysical neutrino source would then be a signal of accelerated hadrons. Each annihilation channel provides a unique neutrino energy spectrum, and since the probability of neutrino detection depends sensitively on its energy, different neutrino signals can be expected from different annihilation channels. Also, since neutrinos interact only weakly with matter, they are insensitive to radiation fields and are accessible to cosmological distance scales. However, the same effect yields low cross sections, and the backgrounds from existing atmospheric neutrinos are significant. For our vectorlike neutrino dark matter candidate, annihilation in the Galaxy into ordinary neutrinos $\nu\bar{\nu}$ may be of significance. During propagation, neutrinos oscillate between flavors, but after traveling across cosmological distances, the coherence between different flavor states is lost and, as they reach Earth, neutrinos become mass eigenstates. These experiments also include limits on the muon flux, which incorporates limits for the $b\bar{b}$, $\tau^+\tau^-$, and W^+W^- channels, for the purpose of comparing with other neutrino telescope experiments. In Fig. 7, we plot the flux as a function of the dark matter mass (neutrino flux in the left panel, muon flux in the right panel) and compare it with the experimental limits from Baikal [73].

D. Direct DM searches at the LHC

DM searches can be performed at the LHC, where in general, the DM particles would be invisible and reveal their presence only as missing transverse energy. The direct searches at the LHC involve looking at the associated particles which come from ISR (initial-state radiation) or from their associated production with the DM candidate. The LHC DM searches concentrate mainly on the mono-X ($X =$ jet, γ, Z, W) signals, where the DM particle is produced either in association with one or more QCD jets, or with a vector boson $V = \gamma$, Z, W. The strongest constraint placed by the recent ATLAS searches on the monojet signal excludes a signal cross section above 19 fb at a 95% C.L. [74]. In our model, the cross sections for the vectorlike neutrino production with jets are small [$\mathcal{O}(0.1$ fb)]; therefore, they safely satisfy the current experimental limits and can only be detected with higher detector sensitivity. However, here we present a more viable detection channel for the vectorlike neutrinos, where they are produced from the secondary decay of charged vectorlike leptons.

IV. COLLIDER SEARCHES

In this section, we will analyze our findings in light of the collider searches for the new exotic vectorlike leptons [75,76]. As already explained in the previous section, the imposition of an extra parity symmetry provides a viable cold dark matter candidate. More explicitly, the lightest neutral vectorlike lepton which is the lightest among the physical mass eigenstates defined in Eq. (23) acts as the good DM candidate. Also, the notable feature of the DM particle is that it is dominantly right-handed and thus can easily yield correct relic density within the 2σ range of Planck's latest relic density value $\Omega_{\rm DM}h^2 = 0.1199 \pm 0.0027$, as we showed in Sec. III. We have shown that there exists ample parameter space which

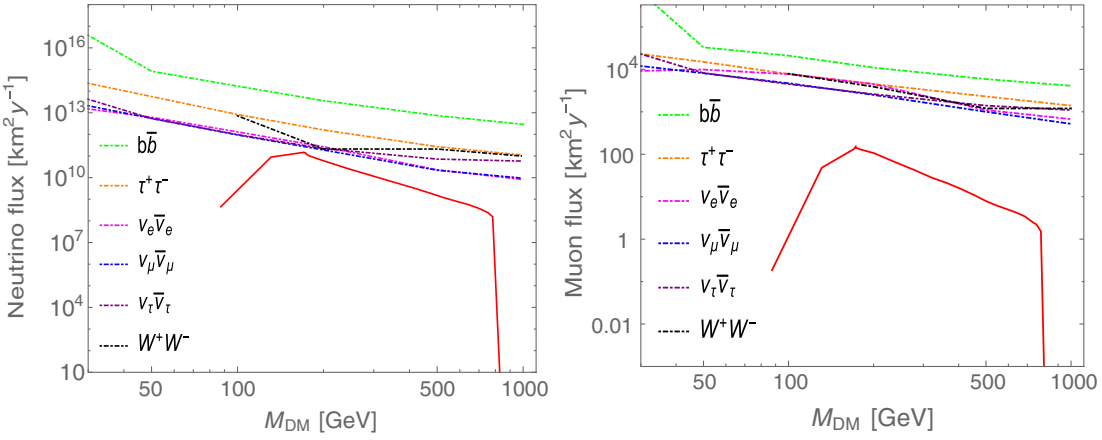

FIG. 7. Neutrino (left) and muon (right) fluxes as a function of dark matter mass (red curve). The dashed curves represent 90% C.L. upper limits from Baikal [73]. We include only points in the parameter space where relic density constraints are satisfied. All the other parameters are fixed at our BP1 values in Table II.

TABLE I. Fixed parameters for all benchmark points.

Yukawa parameters	Y'^{e}_{L}	$\tilde{Y}'^{e}_{L}$	Y'^{e}_{R}	$\tilde{Y}'^{e}_{R}$	Y'^{ν}_{L}	Y'^{ν}_{R}	$\tilde{Y}'^{\nu}_{L}$	$\tilde{Y}'^{\nu}_{R}$	h'_L	h''_L	h''_R	κ_1 [GeV]
Value	0.1	0.0	0.0	2.5	1.5	0.04	0.1	0.1	0.8	0.7	0.0	246

satisfies all the DM constraints, including relic density and direct-detection data. However, in addition to the DM vectorlike neutrino, the model consists of extra charged vectorlike (VL) leptons, which can decay into final states including DM. An obvious question would be whether, in the allowed parameter region, there could be any signature of these charged leptons in the existing or upcoming collider experiments.

A. Benchmark points

At this point, we would like to review our choice of benchmark points and explain their plausibility. The vectorlike lepton sector of this model depends upon 14 parameters, among which 12 are the Yukawa couplings connecting the nonstandard charged and neutral leptons (Y_L, Y_R, h_L, and h_Rs) to the Higgs bosons, and the rest are the two bare mass terms (M_L and M_R) for vectorlike leptons. We are interested in the region of parameter space where the DM constraints are satisfied and the VL charged leptons are kinematically accessible both to the LHC with $\sqrt{s} = 14$ TeV and at the proposed e^+e^- international liner collider with $\sqrt{s} = 1$ TeV. In view of these, we first fix most of the Yukawa couplings, and we choose different masses for the VL leptons by varying the bare mass parameters, M_L and M_R. It can be noted that the dominant right-handed nature of the DM (ν_1) and the lighter charged VL lepton ($E_2^{\pm}$) demand a relatively smaller M_R than M_L, for both to acquire masses of the order of a few hundred GeV. With this procedure, for a particular choice of DM mass, we get the correct relic density and direct-detection cross section by mainly tuning the Yukawa parameter h'_R. In Table I, we display the values for the Yukawa coupling parameters of our choice, while in Table II, we give the masses of the lightest charged and neutral leptons, and the corresponding relic density and direct-detection cross section, both spin dependent and spin independent, for the three benchmark points of our interest.

1. Higgs signal strengths

In our model, the lightest *CP*-even scalar state resembles the 125 GeV Standard-Model-like Higgs boson discovered at the LHC. Therefore, it is important to check the signal strengths for the production and decays of this Higgs state in this model relative to the current experimental data. Since the tree-level couplings of the lightest *CP*-even Higgs boson with all the Standard Model particles remain unchanged, we do not expect any deviations in the tree-level decay channels of this Higgs boson from that of the Standard Model one. The gluon fusion production is not affected by leptons, but the loop-induced decay modes of Higgs into the diphoton channel will get extra contributions from singly and doubly charged scalars and also from the exotic vectorlike charged lepton loops. The new VL charged leptons are expected to contribute destructively (with respect to the dominant WW loop contribution), as the fermion loop comes with a negative sign, while the charged scalar loops may enhance or suppress the decay depending on the sign of the coupling of the charged scalars to the lightest *CP*-even Higgs boson. For brevity, we do not give the general expression for the Higgs to diphoton decay width, which can, however, be found in literature [77–80]. The test is done only for the charged lepton mass values chosen in the above-mentioned benchmark points, while the singly and doubly charged scalar masses are chosen as 243 and 305 GeV, respectively, throughout the analysis. The implications of these charged scalars in our collider study will be mentioned later. The Higgs couplings to these nonstandard charged scalars and the VL leptons are fixed for all benchmark points, since the Yukawa parameters are kept fixed. Moreover, there is no additional contribution to Higgs production through gluon fusion; hence only the ratio of the partial decay width Higgs-to-diphoton channel between the model prediction and that of the SM value represents our signal strength. According to the latest result from LHC run II at 13 TeV, the Higgs-to-diphoton signal strength is $\frac{\mu_{\rm exp}}{\mu_{\rm SM}} = \frac{[\sigma(pp\to h)\mathrm{BR}(h\to\gamma\gamma)]_{\rm exp}}{[\sigma(pp\to h)\mathrm{BR}(h\to\gamma\gamma)]_{\rm SM}} = 0.85^{+0.22}_{-0.20}$ [81]. For our

TABLE II. Benchmark points for vectorlike leptons, including masses with corresponding DM relic density and direct-detection cross section.

Benchmark points	h'_R	M_L (GeV)	M_R (GeV)	$M_{\rm DM}$ (GeV)	$M_{E_2^{\pm}}$ (GeV)	$\Omega_{\rm DM}h^2$	$\sigma_{\rm SD}$ (pb)	$\sigma_{\rm SI}$ (pb)
BP1	0.045	1000	275	173	275	0.116	1.3×10^{-4}	2.55×10^{-11}
BP2	0.033	2000	350	258	350	0.112	4.3×10^{-5}	4.3×10^{-12}
BP3	0.032	2500	400	299	400	0.117	3.1×10^{-5}	2.42×10^{-12}

benchmark points, the signal strengths are—for BP1, BP2, and BP3, respectively—0.59, 0.73, and 0.80, which are all within the 2σ range of experimental data.

B. Searches at the LHC

In this section, we consider the pair production of the lightest charged vectorlike leptons, namely $E_2^{\pm}$, at the LHC:

$$pp \to E_2^+ E_2^-. \tag{24}$$

Instead of scanning over the multidimensional parameter space, we choose three benchmark points which are allowed by the constraints coming from the dark matter relic density and direct-detection cross section.

In the chosen parameter region, these charged leptons can only decay to a SM W boson in conjunction with the DM particle (ν_1) with 100% branching fraction: $E_2^{\pm} \to W^{\pm}\nu_1$, thus leading to a $W^+W^- + \not{E}_T$ final state, where $\not{E}_T$ arises due to the presence of a heavy neutral ν_1 particle, which is the cold dark matter candidate. Depending upon the decay mode of the Standard Model W boson, there are three possible final states:

$$\begin{aligned}
&(a)\ 2\ell^{\pm} + 0j + \not{E}_T \quad (\text{both } W\text{'s decay leptonically})\\
&(b)\ 1\ell^{\pm} + 2j + \not{E}_T \quad (\text{one } W \text{ decays leptonically;}\\
&\qquad \text{the other one decays hadronically})\\
&(c)\ 0\ell^{\pm} + 4j + \not{E}_T \quad (\text{both } W\text{'s decay hadronically}),
\end{aligned} \tag{25}$$

where $\ell = e$, μ, and j corresponds to light quark jets. At this point, it should be mentioned that the final states closely resemble the pair production of SM W. However, in this case, one may expect to see some deviation in the shape of the $\not{E}_T$ distribution compared to that of the SM W-pair signal. This change may be attributed to the fact that for the signal, the missing transverse energy comes from the massive neutral particle, whereas in the SM background, almost massless neutrinos are the decay products. Hence, we expect that the SM processes which contribute to the background for the SM W-pair signal will also play the same role in our signal process. Although the cross sections are higher for the final states (b) and (c), listed in Eq. (25), these final states are difficult to measure at the LHC because of the large background contributions mainly arising from $t\bar{t}$, single top, $W^{\pm}$ + jets and other diboson productions, all of which are difficult to suppress. Therefore, the dileptons and missing transverse energy ($2\ell^{\pm} + \not{E}_T$) final state is the only possible channel to probe this vectorlike heavy lepton signal at the LHC. As already mentioned, our signal process mimics the exact SM W-pair production process, but with a different $\not{E}_T$ spectrum. Hence, it is expected that the application of the same event selection method for SM W pair production to our signal process will suppress the other dominant SM backgrounds to the final state (a). Therefore, to have an overview of signal significance, throughout our analysis, we only consider the SM W^+W^- process as the dominant background.

For our analysis, we supplement the model in Ref. [62] with VL leptons, using FeynRules [63], which gives the UFO model files required in `Madgraph5` [82] to generate the signal events at the LO parton level. The SM background events are also generated using `Madgraph5`. The unweighted parton level events are passed through `Pythia` (v6.4) [83] to simulate showering and hadronization effects, including fragmentation. The detector simulation is done using `Delphes` (v3) [84]. Finally, we perform the cut analyses using `MadAnalysis5` [85]. At this point, we would like to mention that at the detector level, the criteria for the isolation of electrons and muons at the final state are performed using the method described in Ref. [86], where electrons are isolated with the `Tight` criterion defined in Ref. [87], and muons are isolated using the `Medium` criterion defined in Ref. [88]. Jets are reconstructed using the anti-k_t clustering algorithm with radius parameter $\Delta R = 0.4$ with minimum $p_T = 20$ GeV, and jets originating from the fragmentation of b hadrons (b jets), if any, are tagged with 85% tagging efficiency, and with 10% and 1% mistagging efficiency for c-quark and light-quark jets, respectively. The leading-order (LO) production cross sections are calculated using the `NNPDF3.0` parton distributions. Before discussing the cut analyses, we show the histograms for the signal and background after imposing the basic cuts described previously.

In Fig. 8, we show the distribution of transverse momentum (p_T) for the hardest (left panel) and second hardest (right panel) charged leptons in the event for the three benchmarks in Table II. As expected, one may note that the signal and background distribution follow almost the same shape, including the visible Jacobian peak at half the W mass ($m_W/2$), except for a little smearing effect mainly in the signal distribution for the highest-p_T lepton, because in the signal case, the decaying W boson gets an extra inherent p_T from its parent vectorlike charged lepton. Thus, it is important to note that we are not allowed to impose larger p_T cuts on the charged leptons than that applied in the SM W-pair production case [86]. The deviation in the distributions of different benchmark points is self-explanatory from their different cross sections. In Fig. 9, we depict the distribution of the p_T of the hardest jet and also the missing transverse energy $\not{E}_T$ for all three benchmark points. Analogous to the p_T distribution of the hardest lepton, the hardest jet also shows a tail at the high-p_T end. But since we have already chosen two lepton final states, the extra jets are only coming from the initial-state radiation (ISR). The common kinematical feature of ISR jets [89] is a crucial dependence on the mass scale that is being probed at the collider experiment, and usually the transverse momentum (p_T) of the ISR jets is higher with heavier BSM particles at the final state. Therefore, an upper

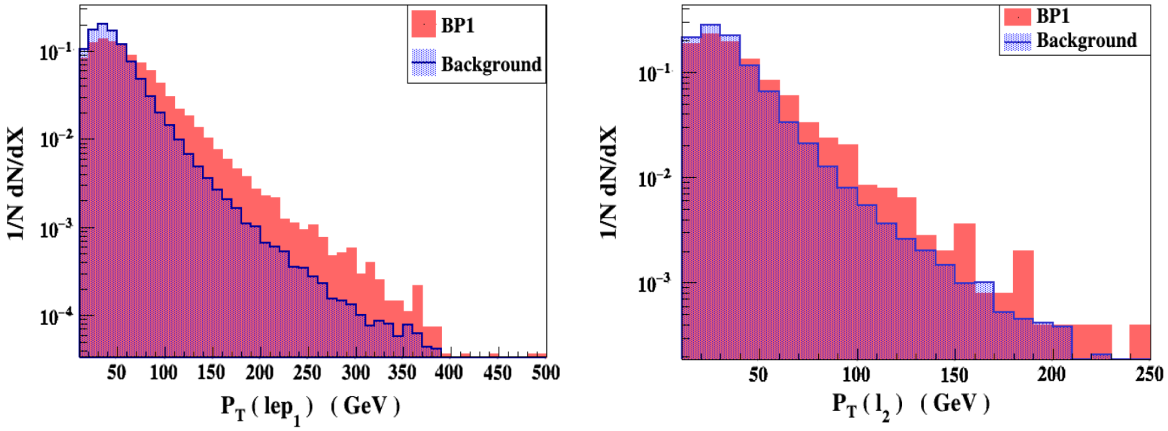

FIG. 8. Distribution for the transverse momentum of the hardest (left panel) and second hardest (right panel) lepton for benchmark point BP1. N is the total number of events before any cut. Distributions for benchmark points BP2 and BP3 are very similar, so we do not plot them as well.

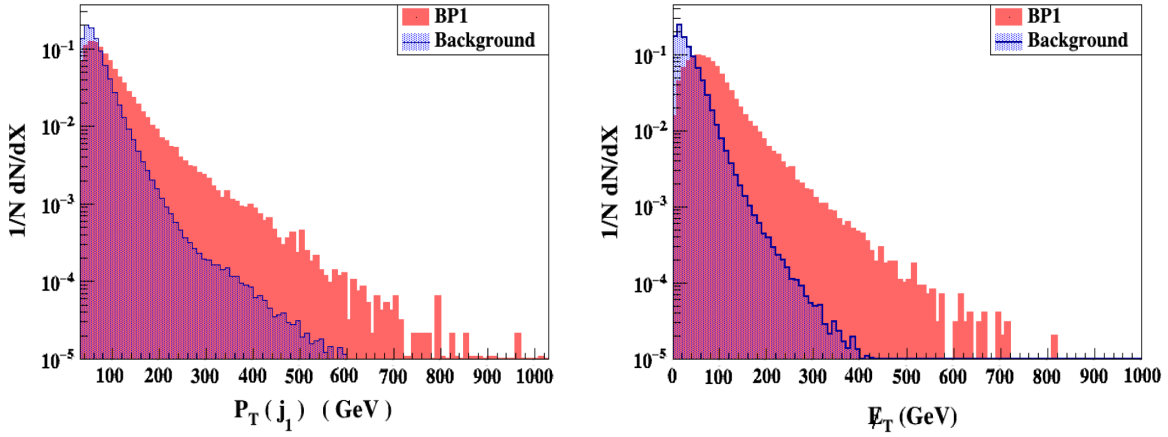

FIG. 9. Transverse momentum of the hardest jet and missing transverse energy distribution for benchmark point BP1. N is the total number of events before any cut. Distributions for benchmark points BP2 and BP3 are very similar, so we do not plot them as well.

cut on the p_T of any extra jets would yield a negative contribution to the signal significance for our final state, since the application of jet veto would be more stringent for the signal than the background. Note that the jet transverse momentum distribution, shown in Fig. 9, is obtained before applying any cuts and with inclusive decay modes of the W boson, and therefore the effect of ISR jets cannot be seen from here. On the other hand, the loss of significance can be gained from the large $\not{E}_T$ in the signal events. As already discussed, for the background events, the missing transverse energy arises only from the neutrinos or the mismeasurement of jets and photons, while, for the signal events, the lightest neutral VL lepton (ν_1) gives the dominant contribution to $\not{E}_T$, which is the stable DM candidate. The large mass range of this ν_1, as shown in Table II, as well as its inherently large p_T due to the mass difference between it and the decaying $E_2^{\pm}$ significantly enhances the $\not{E}_T$ for the signal events. Therefore, one can expect that demanding missing transverse energy $\not{E}_T > 60$ GeV may help in suppressing the background and simultaneously improving the signal significance.

We now discuss the effect of selection cuts imposed over the basic cuts. It should be mentioned here that the analysis is done for a LHC run at 14 TeV, and the expected reach of integrated luminosity is 3000 fb^{-1}. Therefore, we seek to

TABLE III. Selection cut requirements.

Cut name	Selection criteria
C1	Number of jets with $p_T(j) > 30$ GeV and $\lvert\eta\rvert < 4.5 = 0$
C2	At least two leptons with $p_T(\ell) > 25$ GeV
C3	Number of additional leptons with $p_T(\ell) > 10$ GeV $= 0$
C4	$\not{E}_T > 60$ GeV
C5	Number of b-tagged jets with $p_T(b) > 20$ GeV $= 0$

TABLE IV. Effective cross section obtained after each cut for both background and signal, and the respective significance reach at 3000 fb^{-1} integrated luminosity at 14 TeV LHC.

		Effective cross sections in fb after cuts					
	Production cross section (fb)	C1	C2	C3	C4	C5	Significance reached at $\mathcal{L}_{\rm int} = 3000$ fb^{-1}
SM background	70940	6608	558.9	558.9	178.2	177.2	…
BP1	138.4	9.43	1.33	1.33	0.69	0.69	2.83
BP2	53	3.69	0.47	0.47	0.22	0.22	0.90
BP3	31	1.94	0.29	0.29	0.15	0.15	0.01

examine the maximum reach of signal significance at 3000 fb^{-1}, with the significance defined by

$$S = \frac{N_S}{\sqrt{N_S + N_B}}, \tag{26}$$

where N_S and N_B represent the number of signal and background events, respectively.

Akin to the selection cuts imposed in Ref. [86], we list the selection cuts that are imposed in our case in Table III.

We then pass our simulated signal and background events through the cut selection and check the corresponding significance reach at the highest possible integrated luminosity that can be attained at the LHC. We sum up this in Table IV. As can be seen from this table, the maximum significance $\sim 3\sigma$ is attained for BP1, which has the largest production cross section for the vectorlike lepton pairs. For the other two benchmarks, the signal significance is rather poor. From this analysis it is very clear that it would be extremely difficult to probe the vectorlike lepton scenario at the 14 TeV LHC run even with the highest possible luminosity attainable at that energy. Thus, we are motivated to look for the same signal process for the same benchmark points at the upcoming International e^+e^- Linear Collider (ILC) experiment.

To conclude this section, we have shown that pair production of VL leptons is not very promising at the LHC, and would require very high luminosity to disentangle the signal from the background.

C. Searches at the ILC

In view of the fact that the plausible signal for probing the lightest charged VL leptons at the LHC seems difficult to observe and may require much higher luminosity than can be reached, we look for the possibility of probing the same signal at the upcoming International Linear Collider (ILC). The ILC is favored for its clean signal and less background noise, which at LHC originates mainly from the QCD processes. At the LHC, higher-order perturbative QCD corrections as well as nonperturbative QCD effects give rise to large systematic uncertainties in theoretical calculations, and hence precision measurements do not seem to be feasible. On the contrary, the initial-state particles (e^- and e^+) at the ILC are pointlike elementary particles and only interact through electroweak interactions with only a few-percent-level modification in radiative corrections. This is why the ILC results provide better precision and thus help the theoretical understanding of the Standard Model signal and background processes, which may also shed some light on the presence of subtle new physics interactions. In addition to this, the ILC will also be furnished with polarized electron and positron beams so that the processes can be completely characterized based on each initial and final polarization state. For the signal process, we consider exclusive leptonic final states, and hence a better significance than at the LHC is naturally expected. In the following section, we perform the analysis for the pair production of the lightest charged VL leptons—namely, $E_2^{\pm}$—at the ILC. Equivalent to Eq. (24), the process of interest in this case is

$$e^+e^- \to E_2^+ E_2^-. \tag{27}$$

To compare with our previous result on the searches at the LHC, here we also consider only the dilepton final state,

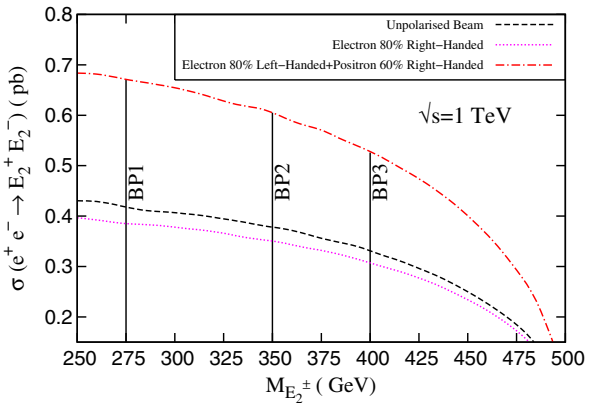

FIG. 10. Signal cross section for different polarization states of incoming electron and positron beams at the ILC for various VL charged lepton masses.

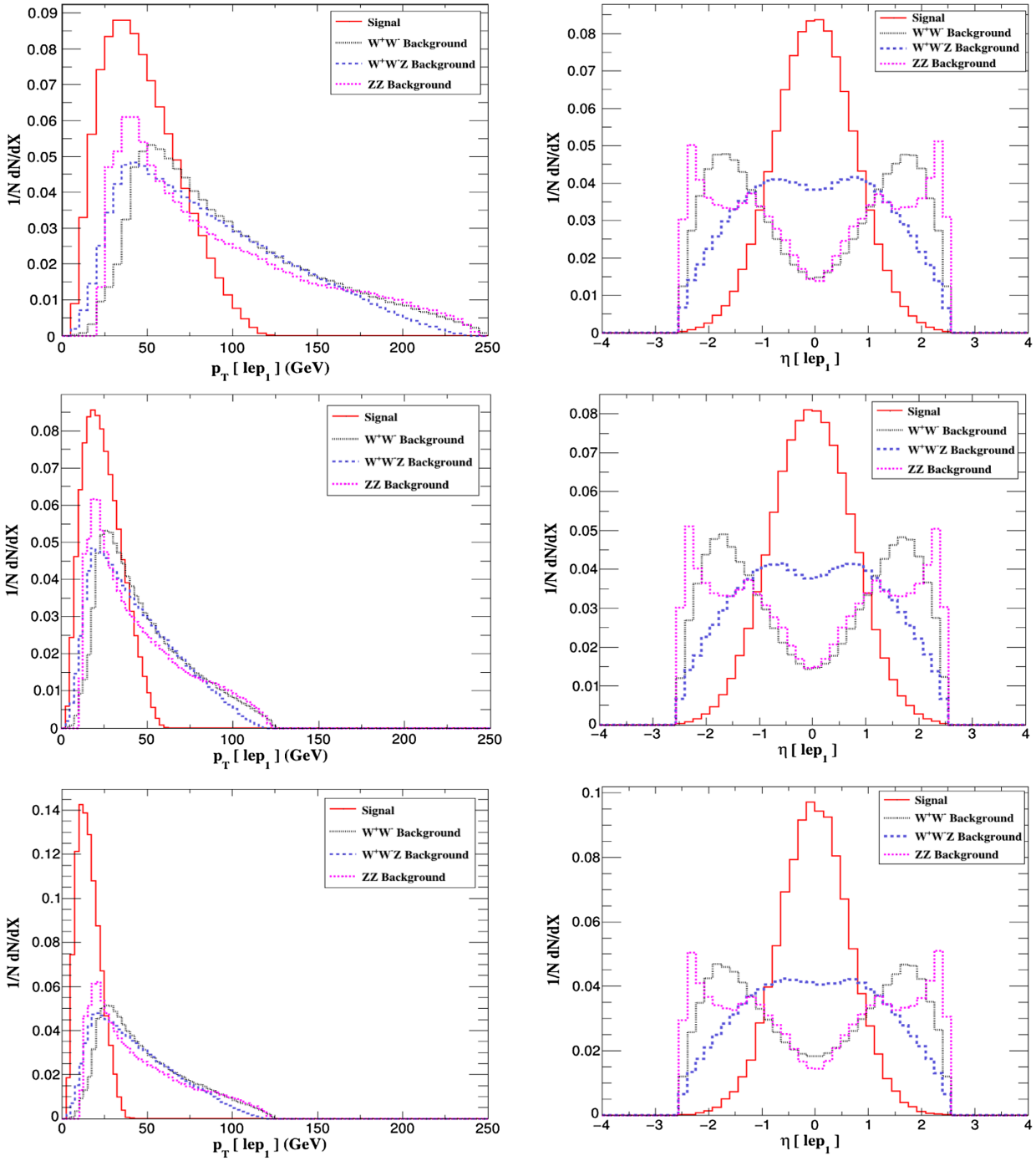

FIG. 11. Transverse momentum and pseudorapidity distribution of the hardest lepton for BP1 and for the combinations (*a*) unpolarized (top), (*b*) both polarized (middle), and (*c*) only electron polarized (bottom).

as mentioned in (*i*) of Eq. (25).[5] In addition to this, we also perform the analysis of VL lepton production using some particular choice of polarization for the incoming electron and positron beams. Explicitly, we consider three distinct combinations [91]:

(a) Both the electron and positron beams are unpolarized.
(b) The electron beam is 80% left polarized, and the positron beam is 60% right polarized.
(c) The electron beam is 80% right polarized, and the positron beam is unpolarized.

For an extensive review on the physics case for the polarized beam at the ILC, we refer to Ref. [92]. In Fig. 10, we show the production cross section for our

[5]A similar study on VL charged lepton searches at the ILC is done in Ref. [90].

process, given in Eq. (27), at the ILC center-of-mass energy 1 TeV. We indicate our chosen benchmark points on the graphs. It is to be noted that the polarization states of the initial electron and/or positron beams change the signal cross section significantly. The highest production cross section can be reached for the combination (*b*), defined previously. The collider analysis is done using `Madgraph5`. In compliance with LHC searches, here too the dominant SM background for dilepton final states is SM W-boson pair production. WWZ and ZZ will also contribute to the background, albeit with small cross sections.

Before imposing selection cuts, we check the distributions of various kinematical variables at the parton level. To do so, some basic cuts are enforced first, such as

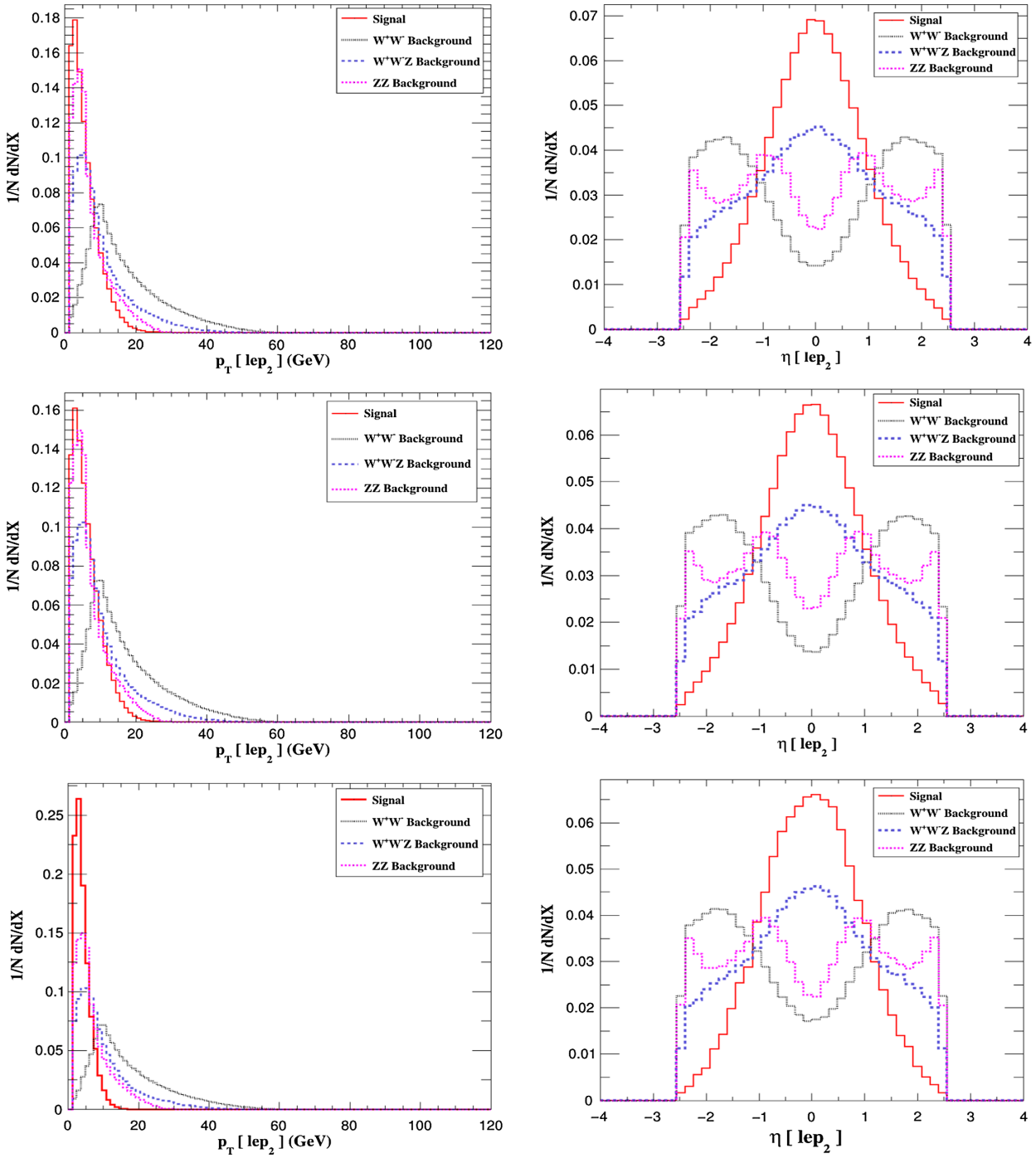

FIG. 12. Transverse momentum and pseudorapidity distribution of the second hardest lepton for BP1 and for combination (*a*) unpolarized (top), (*b*) both polarized (middle), and (*c*) only electron polarized (bottom).

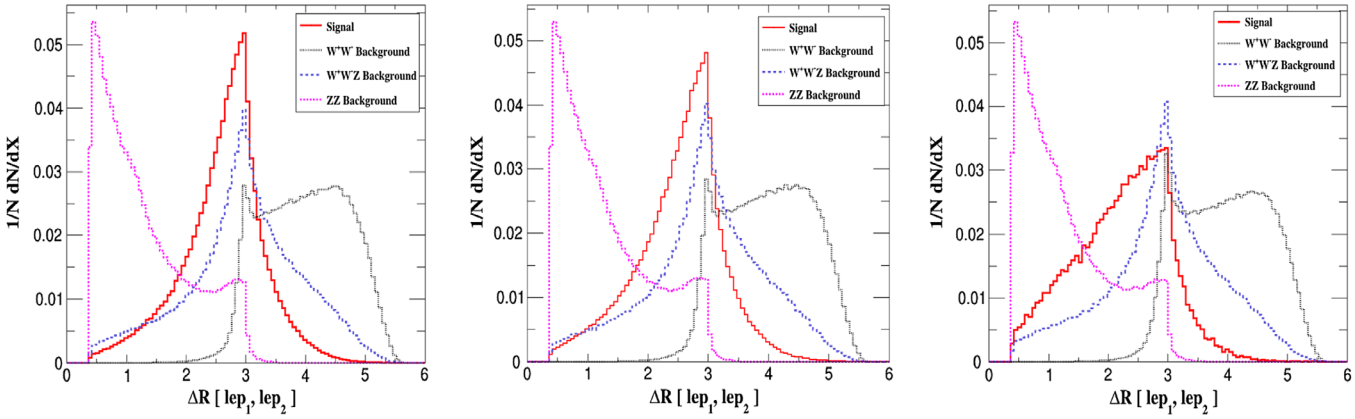

FIG. 13. ΔR distribution of the two leptons for BP1 and for combination (a) unpolarized (left), (b) both polarized (middle), and (c) only electron polarized (right).

(1) The minimum transverse momentum of the charged lepton at the final state should be greater than 10 GeV ($p_{T\ell} > 10$ GeV).
(2) The pseudorapidity of each charged lepton must be within 2.5 ($|\eta_\ell| < 2.5$).

In Fig. 11, the transverse momentum (p_T) and pseudorapidity (η) distribution for the hardest lepton in the final state is shown for all three polarization combinations. The same is shown in Fig. 12, but for the second hardest lepton. We mention here that as an example plot, we only show the distributions for our first benchmark point (BP1), which is the most promising for the experimental detection of our chosen process.

The point to be noted here is that for all the cases, the lepton p_T spectrum for the SM background is relatively harder than that of the signal distribution. This feature can be understood from the fact that for a SM background, leptons originate from the direct-production $W^\pm$ bosons, whereas in the signal process they come from the cascade decay of heavy leptons $E_2^\pm$. This also explains why the pseudorapidity distribution of the leptons is mostly central for the signal, unlike the WW and ZZ cases, where leptons show peaking behavior at large pseudorapidities. However, due to the three-body kinematics of the WWZ process, the pseudorapidity distribution of leptons coming from this process are evenly distributed over the full rapidity range (-2 to $+2$). Keeping this in mind, one can also similarly interpret the distribution of ΔR between the two leptons, which we show in Fig. 13, where ΔR is defined as the measure of angular separation between the two charged leptons by means of their difference in pseudorapidity (η) and azimuthal angle (ϕ): $\Delta R = \sqrt{(\Delta\eta)^2 + (\Delta\phi)^2}$. Both of the charged leptons are generated from one single Z boson for a ZZ background, and therefore the separation is less than the signal and a WW background, where the leptons come from two W's with large angular separation.

At this point, it is worth mentioning that the dilepton final state may also arise from pair production of the singly charged scalar states. The charged Higgs masses only depend on the scalar quartic coupling of Eq. (16) and are independent of the parameter space that we chose for our benchmark points in VL lepton searches. But the production cross section times the branching ratio to dilepton final states is much lower than what we get from E_2 pair production, and so it contributes negligibly to final significance.[6] In this respect, it should also be mentioned that the same recipe also applies to our studies for the LHC searches, but similar to this case, the effective cross section for the pair production of singly charged scalars decaying to dilepton final states at the LHC is too small to add anything to the final signal significance.[7]

Investigating the distributions of the above-mentioned kinematic variables, we choose our final selection cuts. First of all, from Fig. 13, one can see a significant deviation in the spectrum of $\Delta R(\ell_1, \ell_2)$ between our signal and the SM background, mainly from ZZ and WWZ processes. We thus select events with dileptons, where the angular separation between the two leptons must satisfy our first selection cut, $2 < \Delta R(\ell_1, \ell_2) < 3.5$. Next, following the distributions in Fig. 11, we see that a choice of the hardest lepton p_T between 25 GeV and 160 GeV along with a pseudorapidity within the central region ($|\eta(\ell_1)| < 1.5$) may enhance the signal significance by considerably reducing the main WW background. However, one should know that these additional cuts are chosen by only analyzing the unpolarized scenario and are kept the same for the other two polarization combinations. The modification of selection cuts according to specific polarization cases will further increase our final signal significance. The last selection cut on the transverse momentum and

[6]The scalar sector of this model can, however, be detected from other interesting final states, but this is beyond the scope of this work and will be addressed in a future project.
[7]A study on the heavier state of the scalar sector of the model at the High Energetic Future Hadron Collider can be found in Ref. [49].

TABLE V. The cuts implemented for ILC searches.

Cut name	Selection criteria
C1	$2 < \Delta R(\ell_1, \ell_2) < 3.5$
C2	At least one lepton with $25 < p_T(\ell_1) < 160$ GeV and $\lvert\eta(\ell_1)\rvert < 1.5$
C3	At least two leptons with $p_T(\ell_2) > 20$ GeV $\lvert\eta(\ell_2)\rvert < 1.5$

pseudorapidity of the second hardest lepton follows the same logic as the selection cut on the hardest lepton. All the selection cuts are displayed in Table V.

The cut flow and the required integrated luminosity for a 5σ discovery reach are given in Tables VI, VII, and VIII, respectively, for polarization combinations (a), (b), and (c) —i.e., for completely unpolarized initial states, states where both the electron (80% left) and positron (60% right) beams are polarized, and states with only a right-polarized electron (80%) beam. The significance is calculated using the same relation given in Eq. (26).

Let us understand the aftermath of selection cuts for all three cases. As expected, the ΔR selection cut (C1) seems quite competent in suppressing mainly the SM background. While almost 75% signal events pass the cut, only 22% of W^+W^- background events remain unaffected. The signal significance is better when the other two cuts (C2) and (C3) are applied on top of (C1). Quantitatively, almost 90% of background events fail to overcome the cut 2 (C2) selection barrier, while around 85% of signal events survive. The last cut (C3), however, may not play a convincing role in enhancing the signal significance, but the requirement of a second lepton is mandatory to avoid other unwanted SM backgrounds.

Reviewing the cut-flow tables, we observe that the required integrated luminosity for a 5σ discovery reach is quite low, about 2–5 fb^{-1}, which can easily be reached even in the first run of the ILC. The best possible channel turns out to be the benchmark point BP1, with both the initial electron and positron beams polarized as 80% left and 60% right helicity states, and where the required integrated luminosity for discovery reach is as low as 2.09 fb^{-1}. All the rest of the benchmarks and beam polarization states are also promising and can easily be tested at the upcoming ILC searches.

Finally, we would like to point out that we have intentionally chosen those benchmark points where the mass difference between $E_2^\pm$ and the DM (or ν_1) is more than 80 GeV so that the secondary W bosons produced from $E_2^\pm$ only decay on shell. However, there are few available parameter points that can survive the 2σ Planck relic density constraints where the mass difference is less than 80 GeV. For such points, E_2 only decays to three-body final states. We choose two example benchmark values consistent with Fig. 4, as shown in Table IX, for which the relic

TABLE VI. Effective cross sections after each cut for both background and signal, and the integrated luminosity required for 5σ significance ($\mathcal{L}_{5\sigma}$) at 1 TeV at the ILC for an unpolarized incoming beam.

		Effective cross section (fb) after the cut			
SM background	Production cross section (fb)	C1	C2	C3	$\mathcal{L}_{5\sigma}$ (fb^{-1})
W^+W^-	56.5	12.62	1.36	1.16	
W^+W^-Z	0.44	0.21	0.057	0.037	
Z Z	2.13	0.46	0	0	
Total background				1.197	
BP1	17	12.31	10.4	8.81	3.22
BP2	14.5	9.44	9.02	7.45	3.89
BP3	12.8	7.68	7.33	5.85	5.16

TABLE VII. Effective cross sections after each cut for both background and signal, and the integrated luminosity required for 5σ significance ($\mathcal{L}_{5\sigma}$) at 1 TeV at the ILC for a both-polarized incoming beam.

		Effective cross section (fb) after the cut			
SM background	Production cross section (fb)	C1	C2	C3	$\mathcal{L}_{5\sigma}$ (fb^{-1})
W^+W^-	162	35.75	3.93	3.35	
W^+W^-Z	1.2	0.64	0.17	0.11	
Z Z	4.4	1.0	0	0	
Total background				3.46	
BP1	27.7	20.58	17.13	14.76	2.09
BP2	23.5	16.1	15.52	13.02	2.44
BP3	20.64	12.89	12.39	10	3.37

TABLE VIII. Effective cross sections after each cut for both background, and signal and the integrated luminosity required for 5σ significance ($\mathcal{L}_{5\sigma}$) at 1 TeV at the ILC for an incoming beam with only the electron beam polarized.

		Effective cross section (fb) after the cut			
SM background	Production cross section (fb)	C1	C2	C3	$\mathcal{L}_{5\sigma}$ (fb^{-1})
W^+W^-	11.7	2.89	0.31	0.27	
W^+W^-Z	0.09	0	0	0	
Z Z	1.4	0.32	0	0	
Total background				0.27	
BP1	15.62	10.99	9.45	7.86	3.29
BP2	13.4	8.3	7.83	6.37	4.08
BP3	11.9	6.85	6.5	5.11	5.16

TABLE IX. Two distinct parameter points where $(M_{E_2^\pm} - M_{\rm DM}) < 80$ GeV, and the corresponding values for relic density with the $E_2^\pm$ pair-production cross section and the integrated luminosity required for 5σ significance ($\mathcal{L}_{5\sigma}$) at 1 TeV at the ILC for the following cases: (a) Both the electron and positron beams are unpolarized (columns 5 and 6). (b) The electron beam is 80% right polarized, and the positron beam is unpolarized (columns 7 and 8). (c) The electron beam is 80% left polarized, and positron beam is 60% right polarized (columns 9 and 10).

$M_{\rm DM}$ (GeV)	$M_{E_2^\pm}$ (GeV)	$Y_L^{\prime\nu}$	$\Omega_{\rm DM}h^2$	(a) $\sigma_{\rm prod}$ (fb)	$\mathcal{L}_{5\sigma}$ (fb^{-1})	(b) $\sigma_{\rm prod}$ (fb)	$\mathcal{L}_{5\sigma}$ (fb^{-1})	(c) $\sigma_{\rm prod}$ (fb)	$\mathcal{L}_{5\sigma}$ (fb^{-1})
160	184	1.8	0.119	8.4	8.65	7.73	9.4	13.44	5.4
173	238	1.7	0.118	15.72	3.06	14.46	3.3	25.15	1.9

density lies within the 2σ Planck limit. In Table IX, we give the masses of both the DM candidate and the vectorlike charged lepton $E_2^\pm$ along with the respective production cross section for $E_2^\pm$ pair production at 1 TeV at the ILC. Note that such points can only be obtained for large Yukawa couplings $Y_L^{\prime\nu} \gtrsim 1.7$, while fixing the other couplings at the values given in Table I and $h'_R = 0.045$. We analyze both sample points for unpolarized beams at 1 TeV at the ILC with the same cuts mentioned previously. The cut analysis indicates that a 5σ signal significance requires only 8.65 and 3.06 fb^{-1} integrated luminosity, respectively, for the two points at 1 TeV at the ILC. Therefore, it is evident that our ILC search prospect is promising regardless of the mass difference between the two states.

Overall, we see that the VL charged leptons, if they are light—~500 GeV or so—have a clearer signature at the ILC than at the LHC, where they are extremely difficult to probe, even with the highest possible reach of integrated luminosity.

V. CONCLUSION

We present a complete and thorough investigation of the effects of introducing vectorlike leptons into left-right symmetric models. Our aim is to adjoin one missing piece, a dark matter candidate, into the model. In keeping with the symmetries of the model, two vectorlike doublets are introduced, one left-handed and one right-handed, together with their mirrors. A discrete parity symmetry forbids mixing of vectorlike particles with ordinary leptons: this is introduced for simplicity, as mixing can occur, but, given constraints from flavor-changing decays such as $\mu \to e\gamma$, only with the third family, and even there the mixing is constrained to be small so as not to spoil low-energy phenomenology results.

However, in the absence of mixing with SM leptons, the vectorlike leptons mix among themselves, and the lightest state (electrically neutral, and mostly right-handed) is stable and can serve as a dark matter candidate. We show that, for a large range of the parameter space, this vectorlike neutrino obeys constraints from the relic density abundance. In direct detection, the limits on spin-dependent cross sections do not restrict the parameter space, while the spin-independent cross section falls below the LUX and XENON100 limits, whereas XENON1T puts pressure on the lighter (70–150 GeV) region of dark matter mass, which lies within its 2σ sensitivity curves, rather than below. For indirect detection, we analyze the annihilation cross section into SM particles and show that it is safely below the Fermi-LAT limits, and the muon and neutrino fluxes coming from cosmic rays also agree with experimental bounds from neutrino telescopes.

Finally, we investigate the distinctive signals of this scenario at colliders. At the LHC, the pair production of the lightest vectorlike charged leptons, each decaying further into a W boson and dark matter yielding $W^+W^- + \not{E}_T$, is analyzed and compared to the background coming from SM W pair production. We devise three benchmarks obeying all dark matter and Higgs signal constraints, and show that, with judicious background cuts and at HL (high luminosity) at the LHC, one benchmark could reach $\sim 3\sigma$ signal-to-background significance. At this point, we advocate the idea of testing our model at an upcoming electron-positron collider experiment (ILC), in particular for our search channel. The ILC experiment is generally preferred over the hadron colliders because of its clean environment and ability to provide high-precision measurements. Here, we mainly opt for the ILC because of its two main special characteristics. First, the final state with VL charged leptons can be easily probed with much less SM background interference, and second, the ILC provides us with its distinct feature of polarized incoming electron and positron beams, which makes the search channel easier to investigate. In particular, we consider three distinct combinations of beam polarizations, named (a), (b), and (c), respectively, for the cases where both incoming beams are unpolarized, where the electron beam is 80% right polarized and the positron beam is 60% right polarized, and where only the electron beam is 80% right polarized with a completely unpolarized positron beam. Since our signal resembles mostly SM W pair production, the enhancement (suppression) in the production cross section with an incoming beam polarization follows the same rules as a SM WW background does. Similarly to the LHC scenario, we illustrate our search strategies using the same benchmark points as before. The dominant background here is also the SM W^+W^- pair production, with small contributions from W^+W^-Z and ZZ. The most convenient

kinematic variables to distinguish the signal from background are the pseudorapidity of the two charged leptons in the final state and specifically the angular separation (ΔR) between them. Strategic cuts on these variables lead to large signal significance for the pair production of vectorlike leptons. Moreover, the choice of the polarized beam combination (b), where the electron beam is 80% left polarized and the positron beam is 60% right polarized, renders the best possible signal significance. A 5σ discovery reach, in this case, can easily be attained even with an integrated luminosity as small as 2 fb^{-1} for the highest-production cross section benchmark BP1. The other polarization combinations are also impressive and can be tested even at the very first run of the ILC.

Our analysis strategy demonstrates the viability of the model prediction both for DM detection and for collider signatures at the upcoming ILC. Our left-right model with dark matter is thus quite predictable and easily testable, perhaps at the HL-LHC, and certainly at the ILC—albeit, given the CM energies available at the linear collider, for relatively light vectorlike leptons, with masses $M \leq 500$ GeV.

ACKNOWLEDGMENTS

M. F. thanks NSERC for partial financial support under Grant No. SAP105354. N. G. would like to thank the Council of Scientific and Industrial Research (CSIR), Government of India for financial support.

APPENDIX: EIGENVALUES FOR THE VECTORLIKE NEUTRINO MASS MATRIX

We list the eigenvectors of the vectorlike neutrino mass matrix given in Eq. (20):

$$
\begin{aligned}
|\nu_1\rangle \simeq & \frac{M_{\nu_1} m'_\nu}{\sqrt{M^2_{\nu_1}(M^2_R + M^2_{\nu_1}) + m'^2_\nu (M^2_L + M^2_{\nu_1})}} |\nu'_L\rangle + \frac{M^2_{\nu_1}}{\sqrt{M^2_{\nu_1}(M^2_R + M^2_{\nu_1}) + m'^2_\nu (M^2_L + M^2_{\nu_1})}} |\nu'^c_R\rangle \\
& + \frac{M_L m'_\nu}{\sqrt{M^2_{\nu_1}(M^2_R + M^2_{\nu_1}) + m'^2_\nu (M^2_L + M^2_{\nu_1})}} |\nu''^c_R\rangle + \frac{M_R M_{\nu_1}}{\sqrt{M^2_{\nu_1}(M^2_R + M^2_{\nu_1}) + m'^2_\nu (M^2_L + M^2_{\nu_1})}} |\nu''_L\rangle \\
|\nu_2\rangle \simeq & \frac{M_{\nu_2} m'_\nu}{\sqrt{M^2_{\nu_2}(M^2_R + M^2_{\nu_2}) + m'^2_\nu (M^2_L + M^2_{\nu_2})}} |\nu'_L\rangle + \frac{M^2_{\nu_2}}{\sqrt{M^2_{\nu_2}(M^2_R + M^2_{\nu_2}) + m'^2_\nu (M^2_L + M^2_{\nu_2})}} |\nu'^c_R\rangle \\
& + \frac{M_L m'_\nu}{\sqrt{M^2_{\nu_2}(M^2_R + M^2_{\nu_2}) + m'^2_\nu (M^2_L + M^2_{\nu_2})}} |\nu''^c_R\rangle + \frac{M_R M_{\nu_2}}{\sqrt{M^2_{\nu_2}(M^2_R + M^2_{\nu_2}) + m'^2_\nu (M^2_L + M^2_{\nu_2})}} |\nu''_L\rangle \\
|\nu_3\rangle = & \frac{1}{\sqrt{2}} (|\nu'_L\rangle + |\nu''^c_R\rangle) \\
|\nu_4\rangle = & \frac{1}{\sqrt{2}} (|\nu'_L\rangle - |\nu''^c_R\rangle).
\end{aligned}
\tag{A1}
$$

[1] R. N. Mohapatra and J. C. Pati, A natural left-right symmetry, Phys. Rev. D **11**, 2558 (1975).

[2] G. Senjanovic and R. N. Mohapatra, Exact left-right symmetry and spontaneous violation of parity, Phys. Rev. D **12**, 1502 (1975).

[3] R. N. Mohapatra and G. Senjanovic, Neutrino masses and mixings in gauge models with spontaneous parity violation, Phys. Rev. D **23**, 165 (1981).

[4] M. Kadastik, K. Kannike, and M. Raidal, Dark matter as the signal of grand unification, Phys. Rev. D **80**, 085020 (2009).

[5] M. Kadastik, K. Kannike, and M. Raidal, Matter parity as the origin of scalar dark matter, Phys. Rev. D **81**, 015002 (2010).

[6] C. Arbelez, M. Hirsch, M. Malinsk, and J. C. Romo, LHC-scale left-right symmetry and unification, Phys. Rev. D **89**, 035002 (2014).

[7] J. Heeck and S. Patra, Minimal Left-Right Symmetric Dark Matter, Phys. Rev. Lett. **115**, 121804 (2015).

[8] C. Garcia-Cely and J. Heeck, Phenomenology of left-right symmetric dark matter, J. Cosmol. Astropart. Phys. 03 (2016) 021.

[9] W.-L. Guo, L.-M. Wang, Y.-L. Wu, and C. Zhuang, The dark matter constraints on the left-right symmetric model with $Z(2)$ symmetry, Phys. Rev. D **78**, 035015 (2008).

[10] W.-L. Guo, L.-M. Wang, Y.-L. Wu, Y.-F. Zhou, and C. Zhuang, Gauge-singlet dark matter in a left-right symmetric

model with spontaneous CP violation, Phys. Rev. D **79**, 055015 (2009).
[11] W.-L. Guo, Y.-L. Wu, and Y.-F. Zhou, Exploration of decaying dark matter in a left-right symmetric model, Phys. Rev. D **81**, 075014 (2010).
[12] E. Ma, Dark-matter fermion from left-right symmetry, Phys. Rev. D **85**, 091701 (2012).
[13] P.-H. Gu, A left-right symmetric model for neutrino masses, baryon asymmetry and dark matter, Phys. Rev. D **81**, 095002 (2010).
[14] M. Nemevsek, G. Senjanovic, and Y. Zhang, Warm dark matter in low scale left-right theory, J. Cosmol. Astropart. Phys. 07 (2012) 006.
[15] R. Kuchimanchi, P stabilizes dark matter and with CP can predict leptonic phases, Eur. Phys. J. C **74**, 2726 (2014).
[16] G. Aad *et al.* (ATLAS Collaboration), Search for high-mass diboson resonances with boson-tagged jets in proton-proton collisions at $\sqrt{s} = 8$ TeV with the ATLAS detector, J. High Energy Phys. 12 (2015) 055.
[17] V. Khachatryan *et al.* (CMS Collaboration), Search for heavy neutrinos and W bosons with right-handed couplings in proton-proton collisions at $\sqrt{s} = 8$ TeV, Eur. Phys. J. C **74**, 3149 (2014).
[18] M. Aaboud *et al.* (ATLAS Collaboration), Search for resonances in diphoton events at $\sqrt{s} = 13$ TeV with the ATLAS detector, J. High Energy Phys. 09 (2016) 001.
[19] CMS Collaboration, Report No. CMS-PAS-EXO-16-018, 2016.
[20] L. Randall and R. Sundrum, A Large Mass Hierarchy from a Small Extra Dimension, Phys. Rev. Lett. **83**, 3370 (1999).
[21] L. Randall and R. Sundrum, An Alternative to Compactification, Phys. Rev. Lett. **83**, 4690 (1999).
[22] K. Agashe, A. Delgado, M. J. May, and R. Sundrum, RS1, custodial isospin and precision tests, J. High Energy Phys. 08 (2003) 050.
[23] K. Agashe, R. Contino, L. Da Rold, and A. Pomarol, A custodial symmetry for $Zb\bar{b}$, Phys. Lett. B **641**, 62 (2006).
[24] D. Guadagnoli, R. N. Mohapatra, and I. Sung, Gauged flavor group with left-right symmetry, J. High Energy Phys. 04 (2011) 093.
[25] C. S. Aulakh, A. Melfo, and G. Senjanovic, Minimal supersymmetric left-right model, Phys. Rev. D **57**, 4174 (1998).
[26] P. Banerjee and U. A. Yajnik, Production and decay rates of excited leptons in a left-right symmetric scenario, Phys. Rev. D **90**, 095023 (2014).
[27] S. K. Garg and C. S. Kim, Vector like leptons with extended Higgs sector, arXiv:1305.4712.
[28] R. Dermisek, E. Lunghi, and S. Shin, Contributions of flavor violating couplings of a Higgs boson to $pp \to WW$, J. High Energy Phys. 08 (2015) 126.
[29] R. Dermisek, E. Lunghi, and S. Shin, Two Higgs doublet model with vectorlike leptons and contributions to $pp \to WW$ and $H \to WW$, J. High Energy Phys. 02 (2016) 119.
[30] R. Dermisek, E. Lunghi, and S. Shin, New decay modes of heavy Higgs bosons in a two Higgs doublet model with vectorlike leptons, J. High Energy Phys. 05 (2016) 148.
[31] R. Dermisek, E. Lunghi, and S. Shin, New constraints and discovery potential for Higgs to Higgs cascade decays through vectorlike leptons, J. High Energy Phys. 10 (2016) 081.
[32] M. J. Dolan, J. L. Hewett, M. Krmer, and T. G. Rizzo, Simplified models for Higgs physics: Singlet scalar and vector-like quark phenomenology, J. High Energy Phys. 07 (2016) 039.
[33] C. Patrignani *et al.* (Particle Data Group), Review of particle physics, Chin. Phys. C **40**, 100001 (2016).
[34] Y. Zhang, H. An, X. Ji, and R. N. Mohapatra, General CP violation in minimal left-right symmetric model and constraints on the right-handed scale, Nucl. Phys. **B802**, 247 (2008).
[35] P. Langacker and S. U. Sankar, Bounds on the mass of W_R and the $W_L - W_R$ mixing angle ζ in general $SU(2)_L \times SU(2)_R \times U(1)$ models, Phys. Rev. D **40**, 1569 (1989).
[36] R. Barbieri and R. N. Mohapatra, Limits on right-handed interactions from SN1987A observations, Phys. Rev. D **39**, 1229 (1989).
[37] S. Patra, F. S. Queiroz, and W. Rodejohann, Stringent dilepton bounds on left-right models using LHC data, Phys. Lett. B **752**, 186 (2016).
[38] M. Lindner, F. S. Queiroz, and W. Rodejohann, Dilepton bounds on left-right symmetry at the LHC run II and neutrinoless double beta decay, Phys. Lett. B **762**, 190 (2016).
[39] G. Beall, M. Bander, and A. Soni, Constraint on the Mass Scale of a Left-Right Symmetric Electroweak Theory from the $K(L)K(S)$ Mass Difference, Phys. Rev. Lett. **48**, 848 (1982).
[40] G. C. Branco, J. M. Frere, and J. M. Gerard, The value of ϵ'/ϵ in models based on $SU(2)_l \times SU(2)_r \times U(1)$, Nucl. Phys. **B221**, 317 (1983).
[41] G. Ecker, W. Grimus, and H. Neufeld, Higgs induced flavor changing neutral interactions in $SU(2)_l \times SU(2)_r \times U(1)$, Phys. Lett. **127B**, 365 (1983).
[42] I. I. Y. Bigi and J. M. Frere, Strong radiative corrections to strangeness changing processes in the presence of right-handed currents, Phys. Lett. **129B**, 469 (1983).
[43] K. S. Babu, K. Fujikawa, and A. Yamada, Constraints on left-right symmetric models from the process $b \to s\gamma$, Phys. Lett. B **333**, 196 (1994).
[44] P. Ball, J. M. Frere, and J. Matias, Anatomy of mixing induced CP asymmetries in left-right symmetric models with spontaneous CP violation, Nucl. Phys. **B572**, 3 (2000).
[45] A. Maiezza, M. Nemevsek, F. Nesti, and G. Senjanovic, Left-right symmetry at LHC, Phys. Rev. D **82**, 055022 (2010).
[46] M. Blanke, A. J. Buras, K. Gemmler, and T. Heidsieck, $\Delta F = 2$ observables and $B \to X_q\gamma$ decays in the left-right model: Higgs particles striking back, J. High Energy Phys. 03 (2012) 024.
[47] S. Bertolini, A. Maiezza, and F. Nesti, Present and future K and B meson mixing constraints on TeV scale left-right symmetry, Phys. Rev. D **89**, 095028 (2014).
[48] V. Bernard, S. Descotes-Genon, and L. Vale Silva, Short-distance QCD corrections to $K^0\bar{K}^0$ mixing at next-to-leading order in left-right models, J. High Energy Phys. 08 (2016) 128.
[49] P. S. B. Dev, R. N. Mohapatra, and Y. Zhang, Probing the Higgs sector of the minimal left-right symmetric model at future hadron colliders, J. High Energy Phys. 05 (2016) 174.
[50] A. Joglekar, P. Schwaller, and C. E. M. Wagner, Dark matter and enhanced Higgs to di-photon rate from vector-like leptons, J. High Energy Phys. 12 (2012) 064.

[51] K. Ishiwata and M. B. Wise, Phenomenology of heavy vectorlike leptons, Phys. Rev. D **88**, 055009 (2013).
[52] R. Dermisek and A. Raval, Explanation of the muon $g-2$ anomaly with vectorlike leptons and its implications for Higgs decays, Phys. Rev. D **88**, 013017 (2013).
[53] G. Aad *et al.* (ATLAS Collaboration), Search for new phenomena in dijet mass and angular distributions from pp collisions at $\sqrt{s}=13$ TeV with the ATLAS detector, Phys. Lett. B **754**, 302 (2016).
[54] A. M. Sirunyan *et al.* (CMS Collaboration), Search for dijet resonances in proton-proton collisions at sqrt(s) = 13 TeV and constraints on dark matter and other models, arXiv:1611.03568 [Phys. Lett. B (to be published)].
[55] S. Kanemura and K. Yagyu, Radiative corrections to electroweak parameters in the Higgs triplet model and implication with the recent Higgs boson searches, Phys. Rev. D **85**, 115009 (2012).
[56] T. Blank and W. Hollik, Precision observables in $SU(2)\times U(1)$ models with an additional Higgs triplet, Nucl. Phys. **B514**, 113 (1998).
[57] M.-C. Chen, S. Dawson, and T. Krupovnickas, Constraining new models with precision electroweak data, Int. J. Mod. Phys. A **21**, 4045 (2006).
[58] S. Chatrchyan *et al.* (CMS Collaboration), A search for a doubly-charged Higgs boson in pp collisions at $\sqrt{s}=7$ TeV, Eur. Phys. J. C **72**, 2189 (2012).
[59] CMS Collaboration, Report No. CMS-PAS-HIG-14-039, 2016.
[60] CMS Collaboration, Report No. CMS-PAS-HIG-16-036, 2017.
[61] M. Fairbairn and P. Grothaus, Baryogenesis and dark matter with vector-like fermions, J. High Energy Phys. 10 (2013) 176.
[62] A. Roitgrund, G. Eilam, and S. Bar-Shalom, Implementation of the left-right symmetric model in FeynRules, Comput. Phys. Commun. **203**, 18 (2016).
[63] A. Alloul, N. D. Christensen, C. Degrande, C. Duhr, and B. Fuks, FeynRules 2.0: A complete toolbox for tree-level phenomenology, Comput. Phys. Commun. **185**, 2250 (2014).
[64] A. Belyaev, N. D. Christensen, and A. Pukhov, CalcHEP 3.4 for collider physics within and beyond the Standard Model, Comput. Phys. Commun. **184**, 1729 (2013).
[65] G. Blanger, F. Boudjema, A. Pukhov, and A. Semenov, micrOMEGAs4.1: Two dark matter candidates, Comput. Phys. Commun. **192**, 322 (2015).
[66] P. A. R. Ade *et al.* (Planck Collaboration), Planck 2013 results: XVI. Cosmological parameters, Astron. Astrophys. **571**, A16 (2014).
[67] E. Komatsu *et al.* (WMAP Collaboration), Seven-year Wilkinson Microwave Anisotropy Probe (WMAP) observations: Cosmological interpretation, Astrophys. J. Suppl. Ser. **192**, 18 (2011).
[68] L. Scotto Lavina (XENON100 Collaboration), Latest results from XENON100 data, in 24th Rencontres de Blois on Particle Physics and Cosmology Blois, Loire Valley, France, May 27–June 1, 2012 (2013).
[69] D. S. Akerib *et al.* (LUX Collaboration), First Results from the LUX Dark Matter Experiment at the Sanford Underground Research Facility, Phys. Rev. Lett. **112**, 091303 (2014).
[70] E. Aprile *et al.* (XENON Collaboration), Physics reach of the XENON1T dark matter experiment, J. Cosmol. Astropart. Phys. 04 (2016) 027.
[71] T. Daylan, D. P. Finkbeiner, D. Hooper, T. Linden, S. K. N. Portillo, N. L. Rodd, and T. R. Slatyer , The characterization of the gamma-ray signal from the central Milky Way: A case for annihilating dark matter, Phys. Dark Univ. **12**, 1 (2016).
[72] M. L. Ahnen *et al.* (Fermi-LAT and MAGIC Collaborations), Limits to dark matter annihilation cross-section from a combined analysis of MAGIC and Fermi-LAT observations of dwarf satellite galaxies, J. Cosmol. Astropart. Phys. 02 (2016) 039.
[73] A. D. Avrorin *et al.* (Baikal Collaboration), Search for neutrino emission from relic dark matter in the Sun with the Baikal NT200 detector, Astropart. Phys. **62**, 12 (2015).
[74] M. Aaboud *et al.* (ATLAS Collaboration), Search for new phenomena in final states with an energetic jet and large missing transverse momentum in pp collisions at $\sqrt{s}=13$ TeV using the ATLAS detector, Phys. Rev. D **94**, 032005 (2016).
[75] R. Dermisek, J. P. Hall, E. Lunghi, and S. Shin, Limits on vectorlike leptons from searches for anomalous production of multi-lepton events, J. High Energy Phys. 12 (2014) 013.
[76] R. Dermisek, A. Raval, and S. Shin, Effects of vectorlike leptons on $h\to 4\ell$ and the connection to the muon $g-2$ anomaly, Phys. Rev. D **90**, 034023 (2014).
[77] M. A. Shifman, A. I. Vainshtein, M. B. Voloshin, and V. I. Zakharov, Low-energy theorems for Higgs boson couplings to photons, Sov. J. Nucl. Phys. **30**, 711 (1979).
[78] J. F. Gunion, H. E. Haber, G. L. Kane, and S. Dawson, The Higgs hunter's guide, Front. Phys. **80**, 1 (2000).
[79] A. Djouadi, The anatomy of electro-weak symmetry breaking: II. The Higgs bosons in the minimal supersymmetric model, Phys. Rep. **459**, 1 (2008).
[80] A. Djouadi, The anatomy of electro-weak symmetry breaking: I. The Higgs boson in the Standard Model, Phys. Rep. **457**, 1 (2008).
[81] ATLAS collaboration, Measurement of fiducial, differential and production cross sections in the $H\to\gamma\gamma$ decay channel with 13.3 fb^{-1} of 13 TeV proton-proton collision data with the ATLAS detector.
[82] J. Alwall, R. Frederix, S. Frixione, V. Hirschi, F. Maltoni, O. Mattelaer, H.-S. Shao, T. Stelzer, P. Torrielli, and M. Zaro , The automated computation of tree-level and next-to-leading order differential cross sections, and their matching to parton shower simulations, J. High Energy Phys. 07 (2014) 079.
[83] T. Sjostrand, S. Mrenna, and P. Z. Skands, PYTHIA 6.4 physics and manual, J. High Energy Phys. 05 (2006) 026.
[84] J. de Favereau, C. Delaere, P. Demin, A. Giammanco, V. Lematre, A. Mertens, and M. Selvaggi (DELPHES 3 Collaboration), DELPHES 3: A modular framework for fast simulation of a generic collider experiment, J. High Energy Phys. 02 (2014) 057.
[85] E. Conte, B. Fuks, and G. Serret, MadAnalysis 5: A user-friendly framework for collider phenomenology, Comput. Phys. Commun. **184**, 222 (2013).

[86] ATLAS Collaboration, Report No. CERN-EP-2016-267, 2017.
[87] ATLAS Collaboration, Report No. ATLAS-CONF-2016-024, 2016.
[88] G. Aad *et al.* (ATLAS Collaboration), Muon reconstruction performance of the ATLAS detector in proton-proton collision data at $\sqrt{s} = 13$ TeV, Eur. Phys. J. C **76**, 292 (2016).
[89] D. Krohn, L. Randall, and L.-T. Wang, On the feasibility and utility of ISR tagging, arXiv:1101.0810.
[90] V. Ari, O. Čakir, and S. Kuday, Pair production of new heavy leptons with $U(1)'$ charge at linear colliders, Int. J. Mod. Phys. A **29**, 1450055 (2014).
[91] A. Vauth and J. List, Beam polarization at the ILC: Physics case and realization, Int. J. Mod. Phys. Conf. Ser. **40**, 1660003 (2016).
[92] H. Baer, T. Barklow, K. Fujii, Y. Gao, A. Hoang, S. Kanemura *et al.*, Report No. ILC-REPORT-2013-040, 2013.